

A Systematic Search for Molecular Outflows Toward Candidate Low-Luminosity Protostars and Very Low Luminosity Objects

Kamber R. Schwarz^{1,2}, Yancy L. Shirley^{1,3}, and Michael M. Dunham⁴

ABSTRACT

We present a systematic single-dish search for molecular outflows toward a sample of 9 candidate low-luminosity protostars and 30 candidate Very Low Luminosity Objects (VeLLOs; $L_{int} \leq 0.1 L_{\odot}$). The sources are identified using data from the *Spitzer Space Telescope* catalogued by Dunham et al. toward nearby ($D < 400$ pc) star forming regions. Each object was observed in ^{12}CO and ^{13}CO $J = 2 \rightarrow 1$ simultaneously using the sideband separating ALMA Band-6 prototype receiver on the Heinrich Hertz Telescope at $30''$ resolution. Using 5-point grid maps we identify five new potential outflow candidates and make on-the-fly maps of the regions surrounding sources in the dense cores B59, L1148, L1228, and L1165. Of these new outflow candidates, only the map of B59 shows a candidate blue outflow lobe associated with a source in our survey. We also present larger and more sensitive maps of the previously detected L673-7 and the L1251-A IRS4 outflows and analyze their properties in comparison to other outflows from VeLLOs. The accretion luminosities derived from the outflow properties of the VeLLOs with detected CO outflows are higher than the observed internal luminosity of the protostars, indicating that these sources likely had higher accretion rates in the past. The known L1251-A IRS3 outflow is detected but not remapped. We do not detect clear, unconfused signatures of red and blue molecular wings toward the other 31 sources in the survey indicating that large-scale, distinct outflows are rare toward this sample of candidate protostars. Several potential outflows are confused with kinematic structure in the surrounding core and cloud. Interferometric imaging is needed to disentangle large-scale molecular cloud kinematics from these potentially weak protostellar outflows.

¹Steward Observatory, 933 N Cherry Ave., Tucson, AZ 85721

²2009-2010 NASA Space Grant Intern. Senior Honors Thesis for the Honors College at The University of Arizona.

³Adjunct Astronomer, The National Radio Astronomy Observatory

⁴Department of Astronomy, Yale University, P.O. Box 208101, New Haven, CT 06520

1. Introduction

The incredible sensitivity of the *Spitzer Space Telescope* has resulted in the study of a new class of very low luminosity objects (VeLLOs). Formally, a VeLLO is defined as a protostar with an internal luminosity of $< 0.1 L_{\odot}$. The initial *Spitzer* testing and validation observations for the Cores to Disk Legacy team (c2d) detected a new low-luminosity protostar in the previously classified starless core L1014 (Young et al. 2004). Follow-up observations revealed that L1014 was indeed a VeLLO with a weak molecular outflow (Bourke et al. 2005) and centimeter continuum emission consistent with a thermal jet (Shirley et al. 2007). Since the discovery of L1014, the c2d project has completed a census of the embedded protostellar population in the nearby ($D < 400$ pc) low-mass star-forming molecular clouds (see Evans et al. 2009 for a summary). The c2d survey is sensitive to bolometric luminosities of $L_{bol} \sim 0.004 \left(\frac{D}{140pc}\right)^2 L_{\odot}$ and can identify essentially all low-mass protostars with accretion rates down to $\frac{dM_{acc}}{dt} = 1.3 \times 10^{-9} \frac{R_{proto}}{1R_{\odot}} \frac{0.1M_{\odot}}{M_{proto}} \left(\frac{D}{140pc}\right)^2 M_{\odot}/yr$ (see Table 1 for the adopted distances to regions observed). The subset of embedded low luminosity protostars ($L_{bol} \leq 1 L_{\odot}$) including VeLLOs were catalogued by Dunham et al. (2008) and provide the most complete collection that may be systematically studied.

The true nature of VeLLOs are a subject of much current research. Some VeLLOs may be protostars in the incipient stages of accretion, the observationally elusive first hydrostatic core phase of their evolution (Larson 1969; see Machida et al. 2008 for a recent theoretical simulation). Alternatively, some VeLLOs may be more evolved protostars which happen to be observed in a low accretion state. Observations of the molecular outflow, a byproduct of magnetized accretion onto a protostar, provide a potential diagnostic to constrain these two possibilities. Molecular outflows may provide a fossil record of the accretion history of the source.

The source IRAM04191+1522 was one of the first discoveries of a low-luminosity source ($L_{int} = 0.08 L_{\odot}$; Dunham et al. 2006) driving a large-scale molecular outflow (André et al. 1999, Belloche et al. 2002). Since the identification of the outflow around the VeLLO L1014, five more VeLLOs have had outflows detected: L1521F (Bourke et al. 2006), MMS126 (Stanke et al. 2006), Per 073 (Hatchell & Dunham 2009), L673-7 (Dunham et al. 2010a), and L1148 (Kaufmann et al. 2011). Four out of the seven VeLLOs drive large-scale outflows that were detected with single-dish telescopes (IRAM04191, L673-7, Per 073, and MMS126), two of the sources (L1014 and L1148) have outflows that are detected only with interferometers (not detected with single-dish), and one source (L1521F) has a near-infrared scattered light nebula indicative of outflow activity but no direct detection of the outflow. In addition, there are now a few objects with interferometrically detected outflows, but no detected

Spitzer infrared driving source: L1448 IRS2E1 (Chen et al. 2010), Per-Bolo 58 (Dunham et al. 2011), L1451-mm (Pineda et al. 2011), and CB17MMS (Chen et al. 2012). These objects are candidates for first hydrostatic cores although follow-up observations are still needed to confirm their status.

From maps of the emission in the molecular outflow line wings, the dynamical age, mass, momentum, and total outflow force may be estimated (see Cabrit & Bertout 1992). Resulting estimates of the average accretion luminosity are typically larger than the observed source luminosity implying that the accretion rate must have been larger in the past (e.g. Dunham et al. 2010a). This is another version of the famous “luminosity problem” for low-mass protostars, elucidated by Kenyon et al. (1990), where protostars are not luminous enough to account for the expected accretion luminosity based on estimates of the protostellar lifetime. A possible solution to this problem is that the accretion rate is variable with time. Modeling of source counts of protostars in different evolutionary stages from the c2d survey indicates that low luminosity protostars may accrete most of their mass over a period of a few 10^5 years through episodic events (see Dunham et al. 2010b). In order to test this hypothesis, comprehensive surveys for molecular outflows around low luminosity protostars and VeLLOs are needed.

The published searches for molecular outflows associated with VeLLOs have been heterogeneous to date toward a very small fraction of the VeLLO population in nearby clouds and cores. In this paper, we present the first systematic survey for large-scale molecular outflows toward the sample of 39 isolated, candidate low-luminosity protostars (including 30 VeLLOs) in the $J = 2 \rightarrow 1$ lines of ^{12}CO and ^{13}CO (see Table 1). Our main goal is to characterize the frequency of kinematically distinct large-scale outflows toward VeLLOs and to determine the properties (mass, age, momentum, force, etc.) of any detected outflows. In §2 we describe the observing techniques and our sample selection. In §3 we analyze the properties of 3 detected outflows in the sample as well as describe the properties of the numerous non-detections. In §4 we discuss the nature of the VeLLO outflows.

2. Observations

Observations were performed on 9 days between December 2009 and March 2011 (see Table 2) using the sideband separating ALMA Band-6 prototype receiver on the 10-m Heinrich Hertz Telescope. This instrument permits simultaneous dual polarization observations of ^{12}CO $J = 2 \rightarrow 1$ and ^{13}CO $J = 2 \rightarrow 1$ in the LSB and USB respectively with a 5 GHz IF. Observations were performed in 4-IF mode (dual polarization and sideband separating) using filter bank backends with 128 channels at 250 kHz resolution (0.34 km/s and 0.32 km/s

at 220 GHz and 230 GHz respectively).

Pointing was carried out using the planets Jupiter, Mars, and Saturn with a typical rms pointing uncertainty of $< 5''$. Position switching observations with a $5'$ OFF position in azimuth were used to calculate the main beam efficiency ($T_{mb} = T_A^*/\eta_{pol}$; Mangum 1993). The calculated efficiencies for each observing session are given in Table 2. Sideband rejections were measured to be > 13 dB and were not corrected for. Variation in η_{pol} likely reflect calibration variations and changes in the coupling between the receiver optics and the telescope between observing seasons.

2.1. Observing the Sample

Our target objects were selected from the catalogue of low luminosity protostars in the Cores to Disk Legacy sample compiled in Dunham et al. (2008) (their Tables 3 - 8). Throughout this paper, we use the region name followed by the source number in parenthesis listed in the tables of Dunham et al. (2008) (i.e. B35A (007)). The Dunham catalog contains 199 sources. All isolated sources ($> 30''$ from a IRAS source) with suitable declinations observable from the Heinrich Hertz Telescope ($\delta > -30^\circ$) from Dunham Table 3 (Cores) and Dunham Table 7 (Ophiuchus), which had not been observed previously, were included in our final target list of 39 sources. We excluded candidates within a beam width, $30''$, of a known IRAS source, since it is unlikely that we will be able to disentangle the outflow from the low luminosity protostar from the stronger IRAS source. We also exclude some sources and regions where known single-dish searches for molecular outflows have already occurred (e.g. IRAM04191 André et al. 1999, L1521F Bourke et al. 2006, L328 Lee et al. 2009, L1014 Bourke et al. 2007, CB130 Kim et al. 2011, and LFAM 26 Bussmann et al. 2007, Nakamura et al. 2011). We exclude sources in Perseus (Dunham Table 4) and Serpens (Dunham Table 8) because those regions have been recently mapped at $\leq 30''$ resolution in transitions of ^{12}CO (Hatchell et al. 2007, Curtis et al. 2010; Burleigh & Bieging in preparation). We did not observe the Lupus and Chamaeleon II regions as they are too far south and those regions are the the subject of a southern hemisphere companion survey (Dunham et al., in preparation). The final observed sample consists of 39 candidate protostars, listed in Table 1. Of this sample, 30 sources are classified as VeLLOs $L_{IR} < 0.1 L_\odot$ and all sources have $L_{IR} < 0.45 L_\odot$.

For each source in Table 1, a 5-point map was obtained with $30''$ spacing and a minimum of 3 minutes absolute reference position switching. Clean OFF positions were found by manually checking for emission free regions using data from the Dame et al. (2001) survey

included in SkyView CO maps¹. Before using an OFF position we integrated for three to four minutes using a second reference OFF to insure that it was truly free of CO emission. A linear baseline was subtracted from all maps and all data were reduced using custom routines in the GILDAS (CLASS and GREG) software package².

2.2. OTF Mapping

We mapped the sources L673-7 (031), L1251-A (045), B59 (022), B59 (023), L1148 (033), L1228 (036), and L1165 (040). The sources were chosen as either known outflow candidates where the outflow properties were uncertain and could be improved or as new outflow candidates based on the existence of line wings in the observed 5-point spectra (§3.1). For each of these sources we created an on-the-fly (OTF) map with dimensions 5' by 5', 4' by 4', or 3' by 3'. For the L673-7 (031) outflow two regions of size 3' by 3' offset by $\pm 120''$ in the directions of the red and blue wings were also mapped. All maps had 10'' row spacing with a scan rate of 10'' per second and were scanned boustrophedonically in the RA and DEC directions multiple times to improve the signal-to-noise in the line wings.

On-the-fly maps were reduced and analyzed using custom routines in the GILDAS software package. A linear baseline was removed from all observations before they were scaled using the calculated efficiency. These scaled V_{pol} and H_{pol} observations were combined and then convolved and re-gridded using a Gaussian-tapered Bessel function (Mangum et al. 2008). The resulting beam sizes were 35.5'' for ^{12}CO and 36.9'' for ^{13}CO . Integrated intensity maps were created using the convolved and re-gridded spectra. The red and blue wings were partitioned into multiple velocity channels with the minimum channel size being the spectral resolution (δV_{chan}). Using these files we generated channel maps for each source with the lowest contour at the two to three sigma level of integrated intensity ($\sigma_{\text{I}} = \langle \sigma_T \rangle \sqrt{\delta V_{\text{chan}} (v_2 - v_1)}$ where $\langle \sigma_T \rangle$ was found by averaging the baseline rms at several points in the map). These channel maps allowed us to discern any large scale outflow structure for the outflow candidates.

¹The SkyView Virtual Observatory <http://skyview.gsfc.nasa.gov>

²<http://iram.fr/IRAMFR/GILDAS/>

3. Results

3.1. Detections & Non-detections

The line properties for the center spectrum of each source are tabulated in Table 3. The ratio of integrated intensities for ^{12}CO to ^{13}CO ranges from 1.06 to 23.3 though the median is just 3.51. This ratio is much lower than the expected value of approximately 50 for optically thin emission (Wilson & Rood 1994); therefore we conclude that the ^{12}CO emission in these regions is typically very optically thick. This agrees with the general shape of line profiles seen in Figures 1 - 10. Some sources display self-absorbed ^{12}CO line profiles with ^{13}CO peaking near the ^{12}CO absorption dip. The ^{13}CO line profiles are typically well fit by Gaussian line profiles with an average $\Delta v = 2.12 \pm 0.98$ km/s. This linewidth is much larger than the sound speed in 10 K molecular gas (0.077 km/s for CO) indicating that the motions are likely characterized by turbulence. Unfortunately, at the velocities of ^{12}CO line wings, ^{13}CO is typically not detected; therefore, we are unable to make a direct optical depth correction to the ^{12}CO line wing emission.

The 5-point maps for each source (Fig. 1-10) were visually classified according to their spectral features (Table 3). Sources consisting of a single component were flagged with an “s” while sources consisting of multiple components were denoted by “mc”. Just over half of the sources have single component ^{12}CO spectra (53.3%) while one third of the ^{12}CO spectra appear to have multiple velocity components (33.3%). Self absorbed sources are distinguished from sources with multiple components by comparing to the ^{13}CO line: sources with ^{13}CO which peaks near the ^{12}CO absorption dip are considered to be self absorbed and are denoted by the flag “sa”. The remaining 13.4% of sources show signatures of self-absorption in ^{12}CO .

Sources displaying evidence of blue or red wings in ^{12}CO are flagged with “bw” and “rw” respectively. Seven sources (23%) have either a prominent blue wing or a prominent red wing. These are the candidate outflow sources that we explore with OTF observations. The known outflow sources L673-7 (031), L1251 (044), and L1251 (045) are successfully recovered as outflow candidates in our visual flagging scheme. The visual search for outflow signatures is challenging because several sources have confused spectra with multiple velocity components. Nearby IRAS sources, despite being more than one beam (30”) away, also contribute to the confusion in some spectra. The sources L673 (027), (028), and (030) are examples of complicated, multi-peaked spectra which appear to show evidence for an outflow, but all three sources are $< 50''$ from IRAS19180+1116 whose outflow likely dominates the spectra shapes in this region. From the spectra in Figures 1 - 10, we visually selected five additional candidates, B59 (022), B59 (023), L1148 (033), L1228 (036), and L1165 (040), to follow up with OTF mapping that show clear evidence of a blue or red wing.

Each candidate protostar in the Dunham catalog is assigned a group number (1 through 6) which indicates the likelihood that the object is an embedded protostar (see Table 1 for the group numbers). Sources in group 1 are verified protostars with the certainty decreasing with increasing group number. The nature of sources in group 6 is very uncertain due to a lack of supporting observations (i.e. no evidence that the source is embedded within a core, etc.). All three of the known outflow sources that we mapped belong to group 1 (L673-7 (031), L1251 (044), and L1251 (045)). There are only two group 1 or group 2 objects in our sample which were not selected as good outflow targets based solely on the appearance of their ^{12}CO spectra: L673 (027) and L1221 (041). Unfortunately both of these sources are nearby ($42''$) strong IRAS outflow sources. As explained above, the kinematics of the L673 (027) region is severely complicated by the IRAS19180+1116 outflow source. L1221 (041) appears to have extended $4.6\mu\text{m}$ emission in the NW-SE direction that is indicative of an outflow, but unfortunately, the large outflow source IRAS22266+6845 to the northwest appears to overlap in orientation. The effect of the IRAS source outflow can be seen in the northernmost 5-point spectra for L1221 (041) although no outflow signature is apparent at the position of the VeLLO. This region has been observed with the BIMA interferometer (Lee et al. 2005) and a very tenuous detection of the VeLLO outflow is indicated. Deeper interferometric imaging is needed of L1221 (041) to confirm this result.

Of the remaining 5 candidate outflow sources that we mapped, all of them belong to group 6 except B59 (023) which is in group 3. Interestingly, B59 (023) is the only of those candidates that shows evidence of an outflow being associated directly with the source (§3.4). Several of the Ophiuchus sources, (191) through (199) excluding (197), were not detected in ^{12}CO ; all of these non-detections are in group 5. This result indicates that those protostellar candidates are not embedded objects and are not associated with molecular gas.

In summary, all of the confirmed outflow candidates reported in the literature and in this survey belong to groups 1, 2, or 3. In the following sub-sections we analyze in detail the properties of the detected and non-detected outflows observed in the OTF maps.

3.2. The Fully Mapped L673-7 (031) Outflow

Dunham et al. (2010a) discovered a large outflow surrounding L673-7 (031) (L673-7-IRS), but were not sure that the full extent of the outflow was mapped. Here, we present a new map which extends the region covered by Dunham and fully map the outflow associated with this VeLLO with higher signal-to-noise. We follow the methodology described in Dunham et al. (2010a) to derive the properties of the outflow. We explicitly show the functional dependence on the inclination in the calculations. Also, when appropriate, we always chose

the lower limit in a calculation such that the final outflow properties represent lower limits to the actual values.

The outflow properties are first calculated per velocity channel per pixel, then summed over those pixels covered by the outflow and all outflow velocity channels in the intervals $[-0.7, 5.3]$, and $[9.3, 16.3]$ km/s (see Figure 11). Note that this velocity interval is more restrictive than the velocity interval used in Dunham et al. (2010a) and is determined by the velocity interval over which we statistically ($> 2\sigma_I$) detect the outflow signature in the map. For each calculated quantity (mass, momentum, etc.), we propagate the statistical errors on a channel-by-channel basis. The dominant source of statistical uncertainty is in the integrated intensity in the map. We do not propagate the distance uncertainty (a systematic error which itself is poorly constrained) into these calculations.

A lower limit of the dynamical time, t_d , was found by dividing the extent of the outflow by the center velocity of the outflow wing relative to the v_{LSR} of the protostar. We measure the extent of the outflow to be $290''$ compared to the $150''$ used by Dunham et al. (2010a). We calculate $t_d = 4.44 \pm 0.23 \times 10^4 \frac{\cos i}{\sin i}$ yr assuming an angular uncertainty of half the beam size ($15''$). Using this value, we find the time averaged mass accretion rate is $\langle \dot{M}_{acc} \rangle = 2.78 \pm 0.14 \times 10^{-7} \frac{\sin i}{\cos^2 i} M_\odot \text{ yr}^{-1}$ resulting in a total protostellar mass accreted of $M_{acc} = \dot{M}_{acc} t_d = 1.23 \pm 0.09 \times 10^{-2} \frac{1}{\cos i} M_\odot$. The resulting lower limit on the time averaged accretion luminosity ($L_{acc} = GM_{acc}\dot{M}_{acc}/R$ with $R = 3R_\odot$) is $L_{acc} = 0.036 \pm 0.003 \frac{\sin i}{\cos^3 i} L_\odot$. The ratio of the outflow-derived accretion luminosity to the internal luminosity is $2.1 \pm 0.7 \frac{\sin i}{\cos^3 i}$ where we have assumed a 30% uncertainty on L_{IR} .

While our calculated numbers are smaller than the values found in Dunham et al. (2010a), we are now confident that with this new map, the full extent of the L673-7 outflow has been mapped. This independent analysis still supports the hypothesis that L673-7 has undergone episodic accretion; however, the discrepancy between the derived average accretion luminosity and the observed internal luminosity has decreased significantly with our new analysis. It must be kept in mind, though, that we have selected lower limits to all derived outflow quantities except for the inclination. The unknown inclination of the outflow is the largest source of systematic uncertainty. Figure 12 shows that the functional dependence of the outflow dynamical time, force, and time-averaged accretion rate with inclination is monotonic for each quantity. For an inclination of $i_o = 34.3^\circ$, the correction factor $\frac{\sin i}{\cos^3 i} = 1$. The probability that the real inclination of the outflow is greater than an inclination i_o is given by $P(i > i_o) = \cos(i_o)$ for randomly oriented outflows. The inclination for which $\frac{\sin i}{\cos^3 i} \approx 1$ corresponds to an 83% confidence interval that the real outflow inclination is larger than $i_o = 34.3^\circ$. Thus, typical inclination angles will be larger than this value and the derived quantities can easily be factors of a few times larger to over an order of magnitude

larger; therefore, any discrepancy between the time-averaged accretion luminosity and the internal luminosity will also increase by the same factor (see §4.1).

3.3. The L1251 (045) Outflow

L1251 (045) was first mapped by Lee et al. (2010) ($L_{IR} = 0.077$); however, only the properties of the larger, more distinct outflow associated with L1251 (044) were calculated ($L_{IR} = 0.156$). L1251 (044) and (045) are labeled as IRS4 and IRS3 respectively in the Lee et al. (2010) paper. In order to determine the properties of this adjacent outflow we re-mapped the L1251 (045) outflow using higher spacial resolution (30" versus 48" in Lee et al.) and with higher signal-to-noise. We use the same method as for L673-7 to derive the outflow properties (§3.2). The velocity intervals for the blue and red wings span from $[-10, -5]$ km/s and $[-1, 0.5]$ km/s. The smaller velocity difference for the red wing is used to avoid integrating over a second velocity component which peaks +3.8 km/s from the v_{LSR} of the primary component (see Figure 13).

The calculated outflow mass, energy and momentum are slightly larger than for L673-7 despite this outflow being less distinct. Assuming a distance of 300 ± 50 pc (see Dunham et al. 2008) we calculate an outflow dynamical time of $t_d = 2.69 \pm 0.23 \times 10^4 \frac{\cos i}{\sin i}$ yr. This outflow has been powered for just more than half as long (at the same inclination) as the L673-7 outflow; therefore, the derived outflow luminosity and force are higher for L1251-A (045) than for L673-7 (031). We calculate $\langle \dot{M}_{acc} \rangle = 6.3 \pm 1.5 \times 10^{-7} \frac{\sin i}{\cos^2 i} M_\odot \text{ yr}^{-1}$. The lower limit on the protostellar mass accreted is $1.7 \pm 0.6 \times 10^{-2} \frac{1}{\cos i} M_\odot$, making the lower limit for the accretion luminosity $L_{acc} = 0.11 \pm 0.04 \frac{\sin i}{\cos^3 i} L_\odot$. The average (minimum) accretion luminosity is a factor of $1.5 \pm 0.7 \frac{\sin i}{\cos^3 i}$ times higher than the observed internal luminosity. For inclinations greater than 34.3° , the discrepancy will become larger (Figure 12).

3.4. A New Potential Outflow Around B59 (023)

We have identified a new potential outflow around the source B59 (023). This source displays line wings from a blue lobe to the southwest direction from the source (Figure 14). This feature has also been confirmed in CO $J = 3 \rightarrow 2$ observations with the ASTE 12m telescope (Dunham et al., in preparation). Unfortunately, the red wing is confused by a powerful outflow associated with 2MASS source J17112317-2724315 to the northeast (see Brooke et al. 2007). It is not clear whether the blue shifted emission actually emanates from B59 (023), or whether we have mapped its full extent.

Since we are only able to discern one wing of this purported outflow, we report the outflow properties found for the blue wing multiplied by two. B59 (023) is assumed to be at the same distance ($D = 125$ pc) adopted by the c2d team for the Pipe Nebula and Ophiuchus complex. The derived outflow luminosity and force are significantly higher than for L673-7 (031) and L1251 (045), in part due to the apparent small dynamical time. B59 (023) is one of the nine sources in our survey that is technically not a VeLLO ($L_{IR} = 0.343 L_{\odot}$). The (minimum) average accretion luminosity is $1.5 \pm 0.5 \frac{\sin i}{\cos^3 i}$ times higher than the observed bolometric luminosity; however, we caution that the derived parameters may be overestimated if the outflow indeed has a longer dynamical time. Given that the region is too kinematically confusing for trustworthy analysis using only a single dish, we believe this source to be a prime candidate for follow-up interferometric observations.

3.5. OTF Map Non-detections

All of the remaining OTF maps were kinematically confused and we were unable to discern any large scale, distinct bipolar outflow structure originating from our sources. The outflow lobes are not obvious from analysis of the channel maps or individual spectra in the HHT maps (see Figures 15-18). Thus, the remaining four sources cannot be classified as outflow candidates based on their ^{12}CO channel maps. B59 (022) is west of (023) and its spectra are also severely confused by the outflow from IRAS17081-2721 (visible across the northern edge of the channel maps). There does appear to be a red lobe to southwest of B59 (022), but the corresponding blue lobe has strong red wing emission overlapping in the same position (see the top two rows of the channel map in Figure 15). The channel maps for L1148 (033) show no distinct structure in the CO wing emission (Figure 16). Outflow sources can be seen in the maps of L1228 (036) and L1165 (040) but the emission is clearly offset and not associated with the candidate protostars in either case (Figures 17 and 18). We calculate the mass sensitivity of our survey using the same technique as for the detected outflows but over an empty portion of the map. Using the map L1148 (033) and assuming a conservative outflow extent which covers half the map, the 3σ limit for a mass detection is $1.38 \times 10^{-3} M_{\odot}$ which is consistent with the uncertainties for the detected outflows. We display the maps of these non-detections for completeness.

4. Analysis & Caveats

Of the 39 sources observed in this survey, three have previously known large-scale outflows. We initially identified five additional protostars as outflow candidates; but of those

five new candidates, only B59 (023) showed evidence of a newly detected candidate outflow although confusion with the strong nearby IRAS17081-2721 outflow makes estimation of its outflow properties difficult. The VeLLO single-dish outflow detection rate is only 2 out of 30 sources or 7% in this survey. Recently, Hatchell & Dunham (2009) and Curtis et al. (2010) separately mapped and analyzed the outflow properties of protostars in the Perseus molecular cloud. Outflow signatures from only one VeLLO was uniquely identified in their maps (Per 073 in Hatchell & Dunham; $L_{IR} = 0.018 L_{\odot}$) although many sources with luminosities approaching $0.1 L_{\odot}$ were detected in both surveys (e.g., Per 071 in Dunham Table 4 which is source 65 in Curtis et al. 2010; $L_{IR} = 0.105 L_{\odot}$). If we include the other previous VeLLO single-dish detections from the literature (IRAM014191, Per 073, and MMS126), then the single-dish detection rate increases to 13% for 38 VeLLOs observed in cores. These detection rates are low and suggest that large scale outflows from VeLLOs in the Dunham catalog are rarely a dominant kinematic feature in the surrounding molecular cloud.

We compare the properties of the detected VeLLO outflows in this survey with those of other known VeLLOs and low-luminosity objects observed from the Dunham catalogue. The outflow properties are taken from the individual paper references for each source (IRAM01491 André et al. 1999, MMS 126 Stanke et al. 2006, L1014 Shirley et al. 2007, L1448-IRS2E1 Chen et al. 2010, Per 071 073 105 106 Curtis et al. 2010, L1251A-IRS3 Lee et al. 2010, L1148-IRS Kauffmann et al. 2011, Per-Bolo-58 Dunham et al. 2011, L1451-MM Pineda et al. 2011, LFAM 26 Nakamura et al. 2011, CB17 MMS Chen et al. 2012). Not all quantities plotted in Figure 19 were reported directly in each paper; therefore, in those cases the quantities were derived using the same equations as in this paper. If a range of values were given, the average value is plotted. Errorbars were rarely reported in the original references and are not shown in the figure. The plotted values in Figure 19 do not make optical depth corrections or inclination corrections. We used the literature values with the exception of MMS 126 from Stanke et al. (2006) whom made an average optical depth correction (factor of 3.5) and assumed an inclination of 57.3° (we have reversed those corrections for comparison).

There is strong evidence that the outflow properties change as protostars evolve from the Class 0 to the Class I phase; namely, Class 0 sources drive faster, more massive molecular outflows than Class I sources (Arce & Sargent 2006). The outflow mass, momentum, and force decrease from the Class 0 to the Class I phase (see Curtis et al. 2010 for a recent summary). The survey of Bontemps et al. (1996) studied low-mass protostars in the same $^{12}\text{CO } J = 2 \rightarrow 1$ transition that we used in this survey toward a sample that spanned bolometric luminosities from 0.2 to $41 L_{bol}$ among sources from a heterogeneous population of cores and clouds. Bontemps et al. found a correlation between the outflow force and bolometric luminosity with Class 0 sources having larger outflow force than Class I sources. Recently, Curtis et al. (2010) performed a similar analysis on the protostellar population

within a single cloud (Perseus) with sources extending to lower luminosities and found similar results for Class 0 and I sources. The slopes and offsets of the Curtis correlations differ from Bontemps correlations, but the trend of the Class 0 outflow force correlation lying above the Class I correlation holds (see Figure 19).

We have plotted the outflow force of the protostars observed in this paper along with VeLLOs and low-luminosity protostars from the Dunham catalogue that were observed in the literature (Figure 19). The Class 0 (solid line) and Class I (dashed line) correlations observed by Curtis et al. (2010) are over-plotted. The three single-dish detections in this paper are generally more consistent with the Class 0 correlation than the Class I correlation. In general, however, when VeLLO outflows from the literature are included, single-dish detections span both the Class 0 and Class I correlations. The VeLLOs that are only detected interferometrically (blue squares are L1014-IRS and L1148-IRS) are more consistent with the Class I correlation. This is a fair comparison since outflows from both VeLLOs were searched for and not detected with single-dish telescopes (Crapsi et al. 2005; Kauffmann et al. 2011, this work - L1148 (032)). This result is consistent with the conclusions drawn by Shirley et al. (2007) that L1014-IRS is a more evolved protostar which was detected with *Spitzer* while in a low accretion state.

The time average accretion rate, time-averaged accretion luminosity, total outflow mass, and dynamical time of the outflow are also plotted in Figure 19. All of the detected VeLLO outflows are less than 10^5 years old. There is a strong positive correlation between the observed outflow mass and the observed dynamical time of the outflow. More luminous sources also tend to have higher mass outflow rates (and therefore higher accretion rates) although the correlation is less well defined. This is not surprising since the accretion luminosity is linearly proportional to dM/dt .

The time-averaged accretion luminosity onto the protostar is larger than the observed internal luminosity for every single-dish detected protostar except for one source (MMS 126). The median ratio of the outflow-derived, time-averaged accretion luminosity and the observed internal luminosity of the protostar at the current epoch (current meaning when observed by *Spitzer*) for all VeLLO outflows detected with single-dish telescopes is 1.8. The average value of the ratio is 17 but is significantly skewed by IRAM04191 which has a ratio of 89 (André et al. 1999). This result is direct evidence for time-variable accretion. As we shall discuss in the next section, there are several caveats that must be addressed, but the L_{acc}/L_{int} values plotted are likely lower limits and should only increase when corrections for optical depth, excitation, and inclination (Figure 12) are made.

These results may be directly compared to theoretical models of mass accretion. One such model is an episodic accretion for VeLLOs where accretion bursts are short-lived events

precipitated by instabilities in the protostellar disks. The recent paper of Dunham & Vorobyov (2012) investigate this scenario using hydrodynamic models of disks with gravitational instabilities (Vorobyov & Basu 2010) coupled with radiative transfer models to analyze the time evolution of the observed protostellar core. In reality, the instability does not have to be purely gravitational in origin but also may be magnetic in origin (e.g. MRI Armitage et al 2001, Zhu et al. 2010, Simon et al. 2011; Tassis & Moushovias 2005). The general nature of the variation of the mass accretion rate with time is an exponentially decreasing function punctuated with short-lived bursts that vary by two orders of magnitude (see Figure 6 of Dunham & Vorobyov 2012). The average mass accretion rate in their example model is $3.7 \times 10^{-6} M_{\odot}/\text{yr}$ over the first 10^5 years after the formation of the protostar. This is a factor of 4.2 times higher than the typical accretion rate in their example model at 10^5 years. These numbers are very similar to the observed ratios of the accretion luminosity derived from the outflow properties to the observed protostellar luminosity in this paper. This is only a single example model and models with a range of differing initial conditions would produce a wider range of average accretion rate ratios. With the caveats in mind which indicate that the observed L_{acc}/L_{int} and therefore $\langle \dot{M} \rangle / \dot{M}_{now}$ is likely underestimated, this result is consistent with a picture of episodic accretion; but other smoothly varying accretion models, such as a model with a purely exponential drop in the accretion rate with time, cannot be ruled out by these observations alone. Advantages of the episodic accretion model are that it is physically motivated and that it is also successful in explaining the distribution of protostars in a bolometric luminosity - bolometric temperature diagram (i.e. it physically explains the original "luminosity problem"; see Figure 8 of Dunham & Vorobyov 2012). The results from this outflow survey provide additional supporting evidence but not definitive evidence of the episodic accretion model.

4.1. Caveats

Despite our sensitive maps in ^{12}CO and ^{13}CO $J = 2 \rightarrow 1$, it may still be very difficult to distinguish the terminal bow shock of the outflow in a complex kinematic environment. Indeed, many of our protostellar candidates are situated in very confusing regions where the observable signature of a weak outflow can easily be lost on large scales. In this sense, the dynamical time is a lower limit to the actual age of the outflows. Parker (1991) and Fukui (1993) have statistically studied outflow ages and compared to the dynamical time and found an up to order of magnitude discrepancy (see Curtis et al. 2010 for a discussion). The impact of this underestimate of dynamical time on the outflow force is more complicated because more mass would also be swept up by the larger outflow. Therefore, the outflow force is unlikely to decrease in direct proportion to the increase in dynamical time. The effect of a

underestimate of the outflow terminal bow shock on the estimates of the average accretion luminosity is also more complicated. If the outflow extends beyond the region estimated from our maps, then the larger outflow age means that more mass has been accreted. However, that change coupled with an increase in the estimate of the dynamical age means that the overall change in the average accretion luminosity may not change drastically from what we have estimated in this paper.

This caveat must be weighed against the uncertainty in the outflow optical depth, excitation temperature, and inclination which will only increase the derived outflow quantities. For instance, if the outflow inclination is increased from 34.3° to 70° , then the outflow force would increase by a factor of 10. Typical corrections for higher excitation temperatures or optical depths are additional factors of a few. Throughout the calculation of outflow parameters in §3, the lower limits were consistently chosen and L_{acc} was calculated for $i = 34.3^\circ$ ($\frac{\sin i}{\cos^3 i} \approx 1$) which corresponds to an 83% confidence interval that the real outflow inclination is larger. Given these factors, it seems very unlikely that the outflow forces plotted for VeLLOs in Figure 19 will decrease.

We find at least factors of 1.5 and 2 difference between the average accretion rate estimated from outflow properties and the observed protostellar luminosity. These ratios are significant at the $> 2\sigma$ level for all three sources. The typical optical depth corrections (factors of a few) and larger inclinations (also factors of a few) will only tend to increase this difference. The accretion luminosity itself is estimated from very rough values of the outflow jet speed, entrainment efficiency, mass loss rate in the wind versus the mass accretion rate, and assumed protostellar radius. A simultaneous change in several of the the assumed parameters listed above (e.g. lowering the typical jet speed from 150 km/s to 75 km/s, increasing the ratio of $\frac{\dot{M}_w}{\dot{M}_{acc}} = 0.2$, and increasing the protostellar radius from 3 to 9 R_\odot) would be required to reconcile the two luminosity estimates for typical optical depth, excitation temperature, and inclination effects.

5. Conclusions

We have systematically surveyed 30 VeLLOs and 9 low-luminosity objects in ^{12}CO and ^{13}CO $J = 2 \rightarrow 1$ with the HHT from the Dunham et al. (2008) catalog of candidate low-luminosity protostars in nearby ($D < 400$ pc) clouds and cores. From five-point maps, we identified five sources as new candidate outflows and made extended on-the-fly ^{12}CO $J=2 \rightarrow 1$ maps of these regions. Only B59 (023) showed evidence of a candidate outflow, despite the red wing being obscured by emission from IRAS 17081-2721. The remaining sources do not show convincing evidence for a large scale outflow in ^{12}CO maps. When combined with

the grid maps for all 39 sources, these results indicate that the distinct kinematic signatures of large-scale outflows are rare (13% single-dish detection rate for VeLLOs) toward sources in the Dunham et al. (2008) catalog. Every candidate protostar from the Dunham catalog with a single-dish detected outflow belongs to the highest confidence group classifications (groups 1, 2, and 3). We also re-mapped two previously detected VeLLO outflows (L673-7 (031) and L1251-A (045)) to find the full extent of the outflows and better determine their outflow properties. Our results indicate that the time averaged accretion luminosity implied by the outflow properties is at least a factor of two larger than the observed internal luminosity. For larger inclinations of the outflow axis, higher gas excitation temperatures, and optical depth corrections this discrepancy will increase. This result is consistent with a picture of episodic accretion for these objects.

In light of the results from our single dish survey, interferometric observations are needed to complete the search for VeLLO outflows. Interferometric observations have the advantage of spatially filtering out much of the large scale structure that is potentially causing confusion in our single-dish survey. The combined results from an interferometric survey and this single dish survey will provide a census of outflow properties and statistics for VeLLOs that will illuminate the history of accretion towards these sources.

Acknowledgments

We thank the staff of the Arizona Radio Observatory including the operators Bob Moulton and John Downey for their assistance with the observations. Partial funding for KS was provided by the Arizona Space Grant Consortium. YLS is partially supported by NSF grant AST-1008577.

REFERENCES

- André, P., Motte, F., & Bacmann, A. 1999, *ApJ*, 513, L57
- André, P., Ward-Thompson, D., & Barsony, M., 2000, In *Protostars and Planets IV*, ed. V. Mannings, A. Boss, S. Russell, 59
- Acre, H. G., & Sargent, A. I., 2006, *ApJ*, 646, 1070
- Armitage, P. J., Livio, M., & Pringle, J. E. 2001, *MNRAS*, 324, 705
- Belloche, A., André, P., Despois, D., & Blinder, S. 2002, *A&A*, 393, 927
- Bontemps, S., André, P., Terebey, S., & Cabrit, S., 1996, *A&A*, 311, 858
- Bourke, T. L. et al., *ApJ*, 633, 129
- Bourke, T. L., Myers, P. C., Evans, N. J., II, et al. 2006, *ApJ*, 649, L37
- Bourke, T. L., Crapsi, A., Myers, P. C., Evans, N. J. II, Wilner, D. J., Huard, T. L., Jørgensen, J. K., & Young, C. H. 2007, *ApJ*, 633, L129
- Brooke, T. Y., et al. 2007, *ApJ*, 655, 364
- Bussmann, R. S., Wong, T. W., Hedden, A. S., Kulesa, C. A., Walker, C. K. 2007, *ApJ*, 657, L33
- Chen, X., Arce, H. G., Zhang, Q., et al. 2010, *ApJ*, 715, 1344
- Cabrit, S., Bertout, C. 1992, *A&A*, 261, 274
- Crapsi, A. et al. 2005, *A&A*, 439, 1023
- Curtis, E. I., Richer, J. S., Swift, J. J., & Williams, J. P. 2010, *MNRAS*, 408, 1516
- Dame, T. M., Hartmann, D., & Thaddeus, P., 2001, *ApJ*, 547, 792
- Dunham, M. M., Evans, N. J., II, Bourke, T. L., et al. 2006, *ApJ*, 651, 945
- Dunham, M. M. et al., 2008, *ApJS*, 179, 249
- Dunham, M. M. et al., *ApJ*, 721, 995
- Dunham, M. M., Evans, N. J., Terebey, S., Dullemond, C. P., & Young, C. H., 2010, *ApJ*, 710, 470

- Dunham, M. M., Chen, X., Arce, H. G., et al. 2011, *ApJ*, 742, 1
- Dunham, M. M., & Vorobyov, E. I. 2012, *ApJ*, 747, 52
- Evans, N. J. II et al. 2003, *PASP*, 115, 965
- Fukui, Y., Iwata, T., Mizuno, A., Bally, J., & Lane, A., 1992, IN *Protostars and Planets III*
- Hatchell, J., Fuller, G. A., & Richer, J. S., 2007, *A&A*, 472, 187
- Huard, T. L. et al. 2006, *ApJ*, 630, 391
- Kauffmann, J., Bertoldi, F., Bourke, T. L., Myers, P. C., Lee, C. W., & Huard, T. L., 2011, *MNRAS*, 416, 2341
- Kim, H. J. et al. 201, *ApJ*, 729, 84
- Kelly, B. C., 2007, *ApJ*, 665, 1489
- Kenyon, S. J., Hartmann, L. W., Strom, K. M., & Strom, S. E. 1990, *AJ*, 99, 869
- Larson, R. B. 1969, *MNRAS*, 145, 271
- Lee, C.-F., & Ho, P. T. P. 2005, *ApJ*, 632, 964
- Lee, Jeong-Eun, et al. 2010, *ApJ*, 709, 74
- Lee, Chang Won, et al. 2009, *ApJ*, 693, 1290
- Machida, M. N, Inutsuka, S.-i., & Matsumoto, T. 2008, *ApJ*, 676, 1088
- Mangum, J. G., Emerson, D. T., & Greisen, E. W. 2007, *A&A*, 474, 679
- Parker, N. D., Padman, R., & Scott, P. F. 1991, *MNRAS*, 252, 422
- Phan-Bao, N., et al., 2009, *ApJ*, 689, L141
- Phan-Bao, N., Lee, C., Ho, P. T. P., & Tang, Y. 2011, *ApJ*, 735, 14
- Pineda, J. E., Arce, H. G., Schnee, S., et al. 2011, *arXiv:1109.1207*
- Shirley, Y. L., et al. 2007, *ApJ*, 667, 329
- Simon, J. B., Hawley, J. F., & Beckwith, K. 2011, *ApJ*, 730, 94
- Stanke, T., Smith, M. D., Gredel, R., & Khanzadyan, T., *A&A*, 447, 609

Tassis, K., & Mouschovias, T. C. 2005, *ApJ*, 618, 783

Vorobyov, E. I., & Basu, S. 2010, *ApJ*, 719, 1896

Young, C H., et al. 2004, *ApJS*, 154, 396

Zhu, Z., Hartmann, L., Gammie, C. F., et al. 2010, *ApJ*, 713, 1134

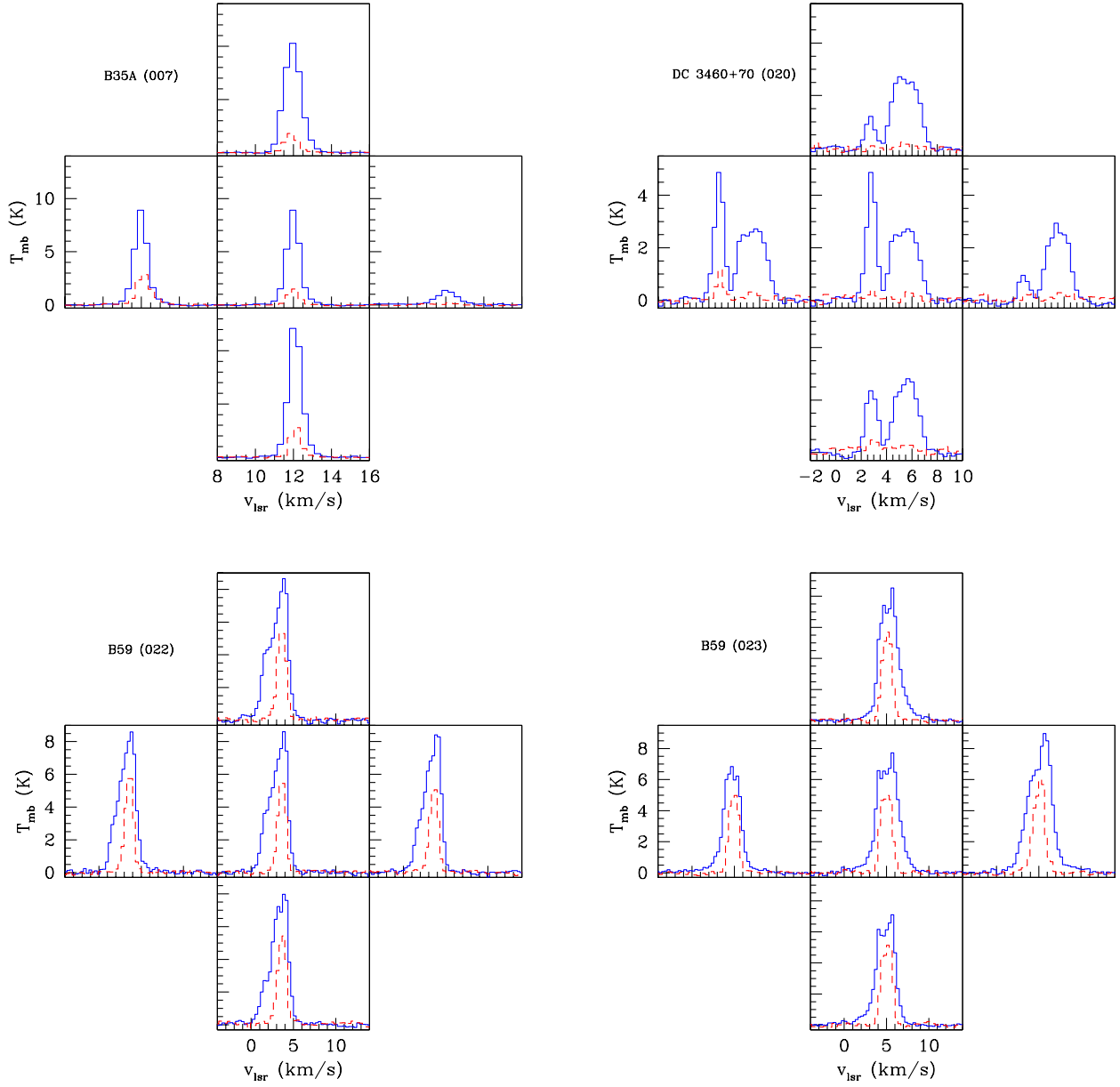


Fig. 1.— 5-point maps of ^{12}CO (solid line) and ^{13}CO (dashed line) 2–1 spectra toward the sources. The offset positions correspond to $30''$ shifts in RA and DEC from the protostar position. The source name is listed in the upper left of each 5-point map.

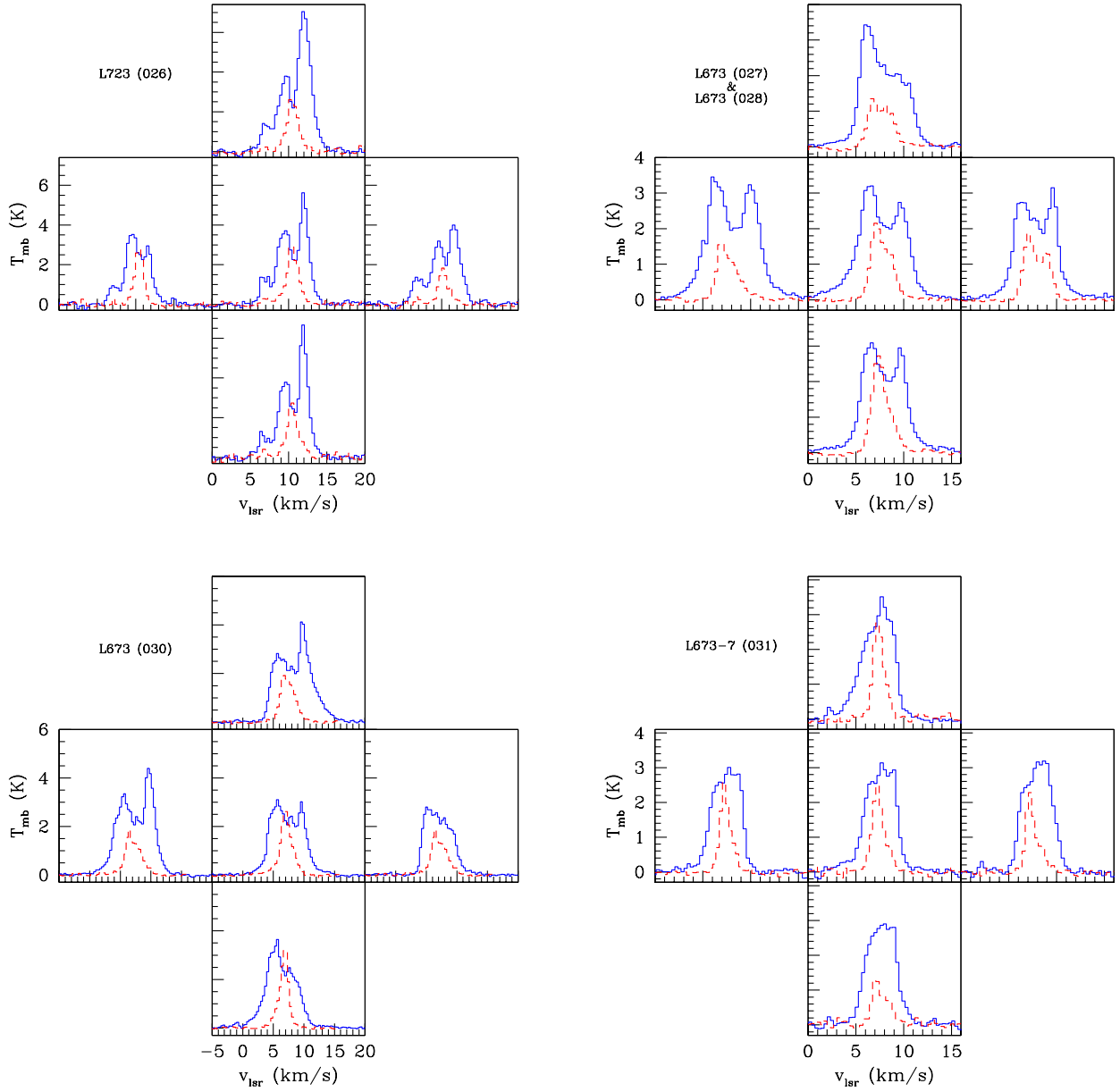


Fig. 2.— 5-point maps of ^{12}CO (solid line) and ^{13}CO (dashed line) 2–1 spectra toward the sources. The offset positions correspond to $30''$ shifts in RA and DEC from the protostar position. The source name is listed in the upper left of each 5-point map. The sources L673 (027) and L673 (028) are separated by only $9.5''$, therefore only 1 map is shown.

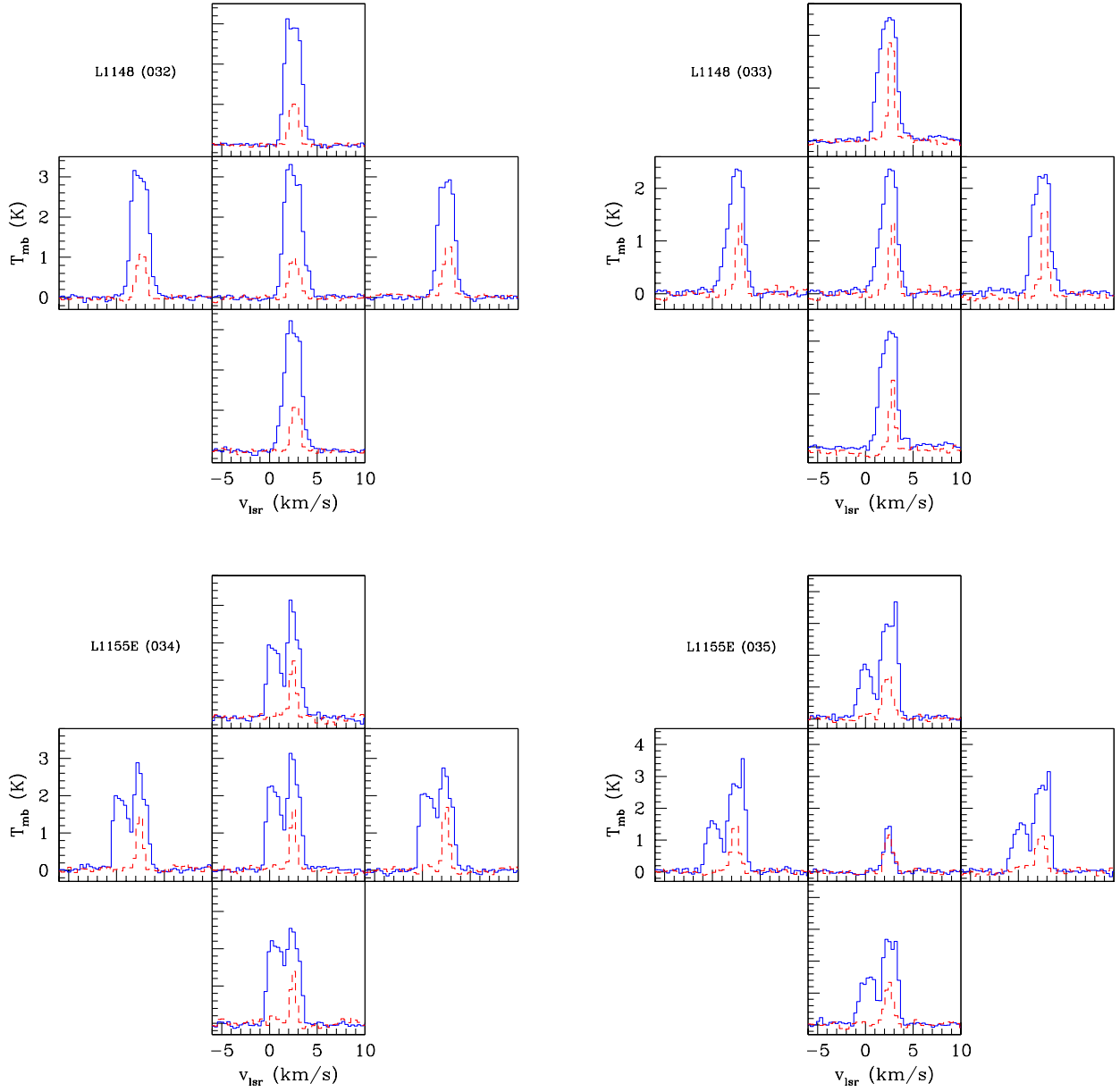


Fig. 3.— 5-point maps of ^{12}CO (solid line) and ^{13}CO (dashed line) 2 – 1 spectra toward the sources. The offset positions correspond to 30'' shifts in RA and DEC from the protostar position. The source name is listed in the upper left of each 5-point map.

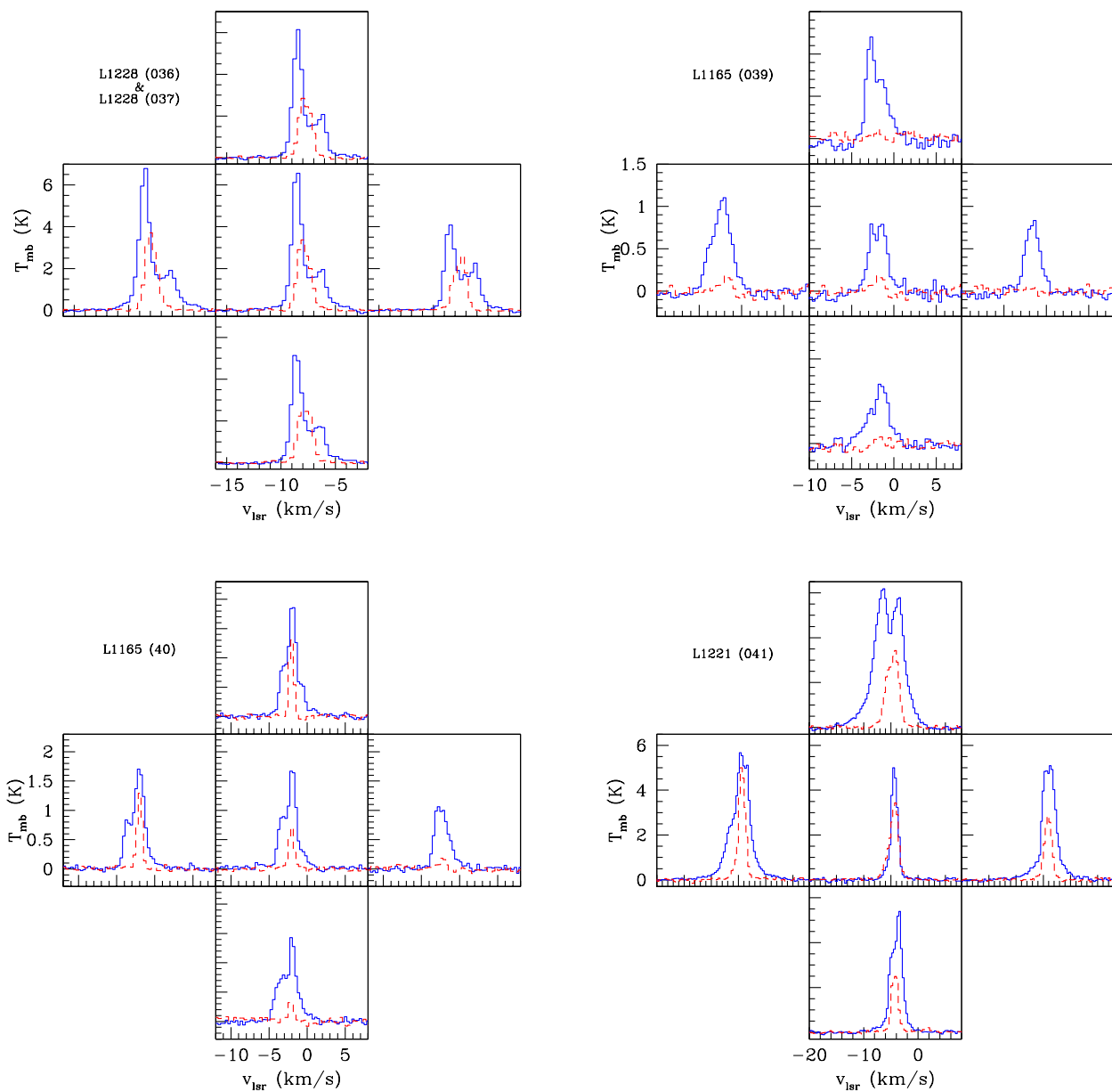


Fig. 4.— 5-point maps of ^{12}CO (solid line) and ^{13}CO (dashed line) 2–1 spectra toward the sources. The offset positions correspond to $30''$ shifts in RA and DEC from the protostar position. The source name is listed in the upper left of each 5-point map. The sources L673 (027) and L673 (028) are separated by only $3.8''$, therefore only 1 map is shown.

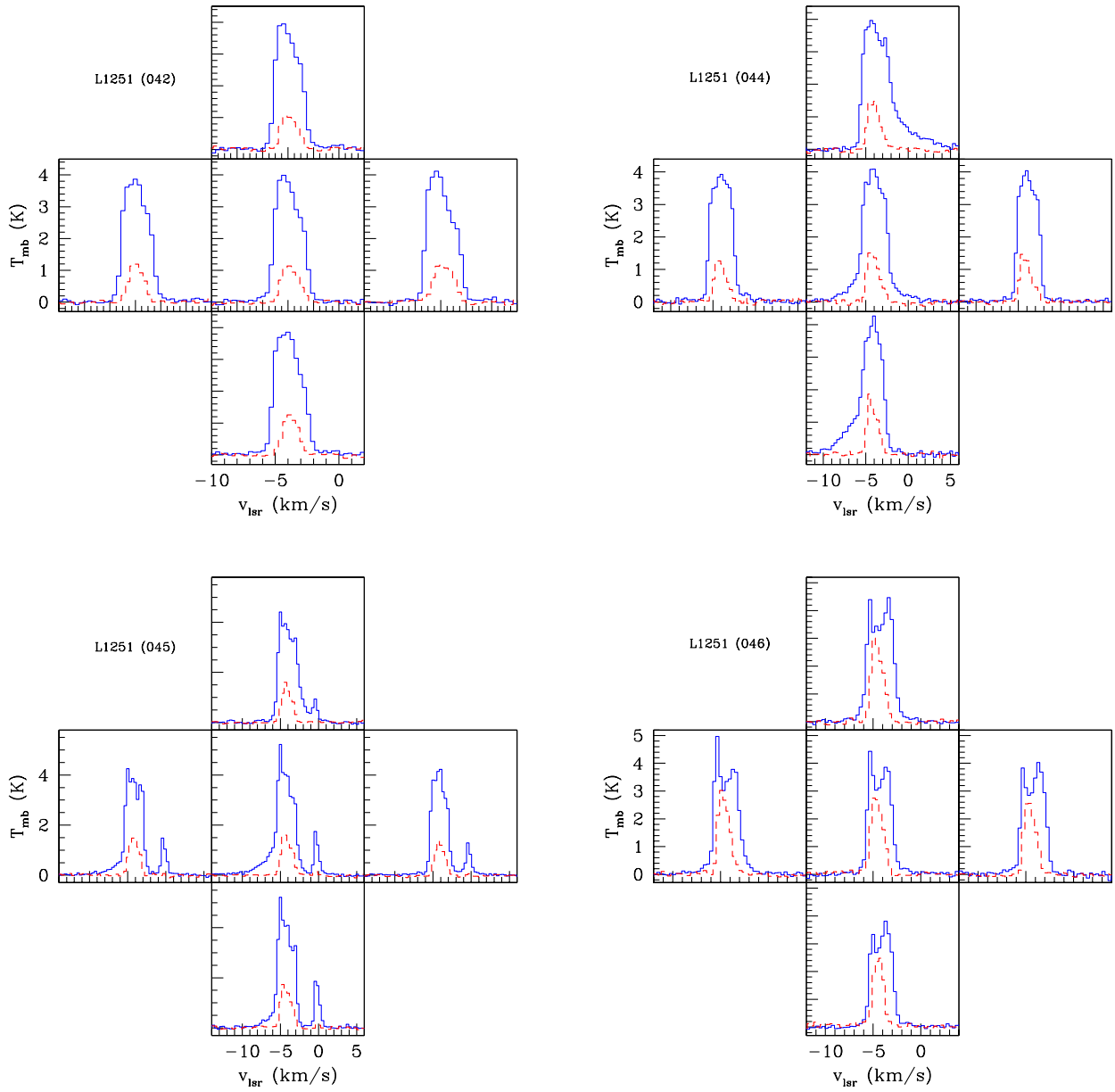


Fig. 5.— 5-point maps of ^{12}CO (solid line) and ^{13}CO (dashed line) 2–1 spectra toward the sources. The offset positions correspond to 30'' shifts in RA and DEC from the protostar position. The source name is listed in the upper left of each 5-point map. L1251 (044) and L1251 (045) are previously detected outflows.

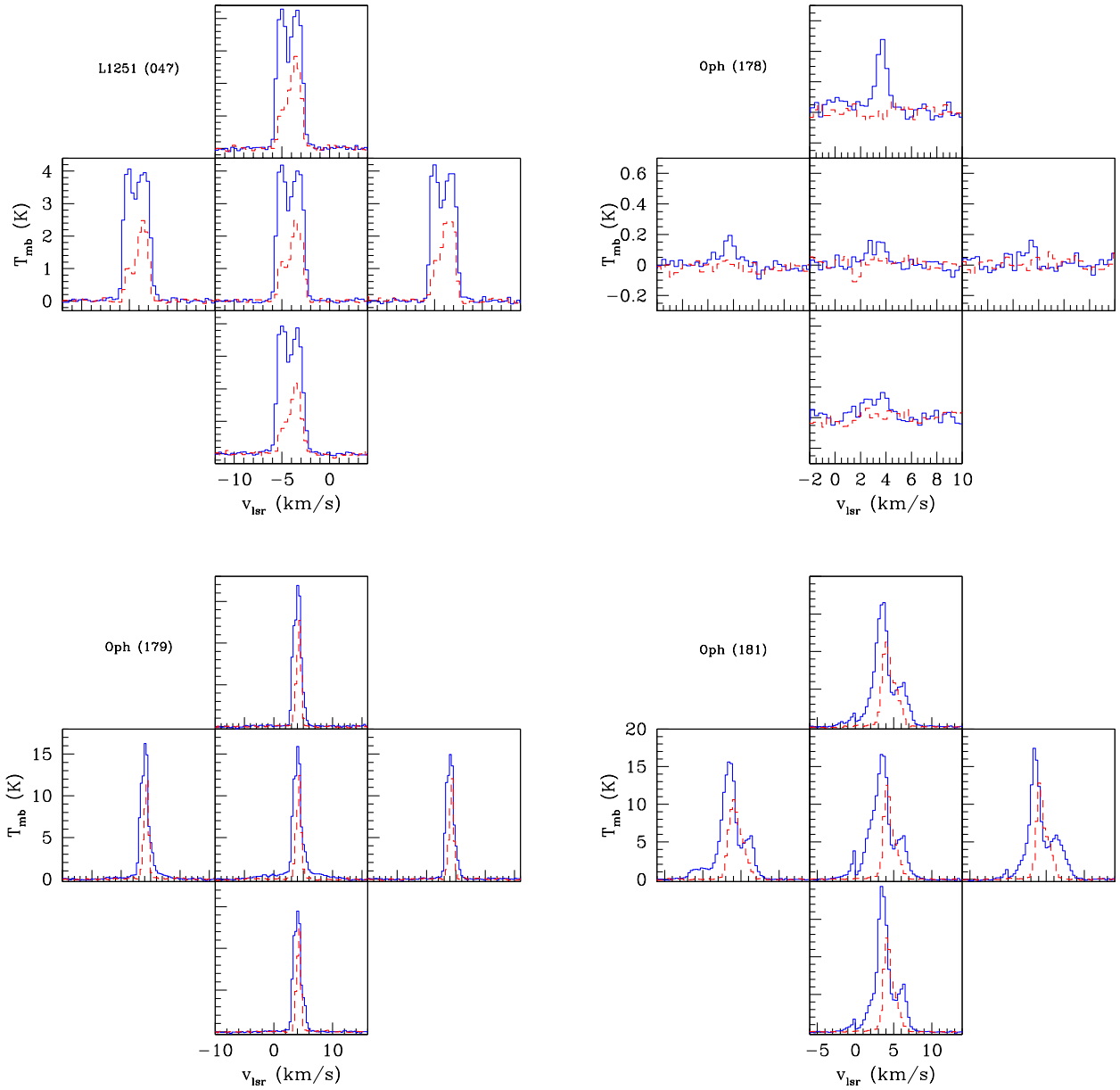


Fig. 6.— 5-point maps of ^{12}CO (solid line) and ^{13}CO (dashed line) 2 – 1 spectra toward the sources. The offset positions correspond to $30''$ shifts in RA and DEC from the protostar position. The source name is listed in the upper left of each 5-point map.

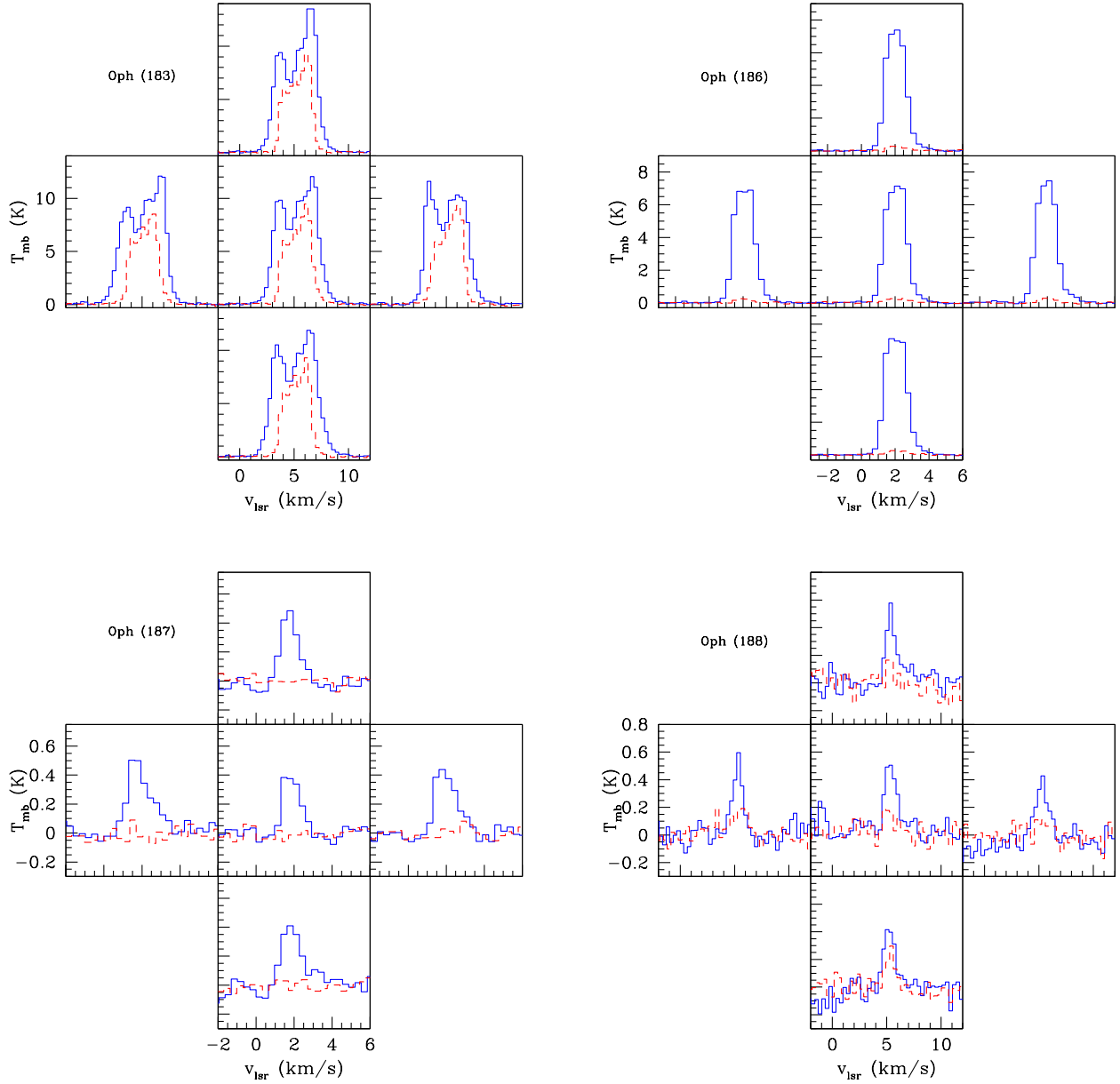


Fig. 7.— 5-point maps of ^{12}CO (solid line) and ^{13}CO (dashed line) 2 – 1 spectra toward the sources. The offset positions correspond to 30'' shifts in RA and DEC from the protostar position. The source name is listed in the upper left of each 5-point map.

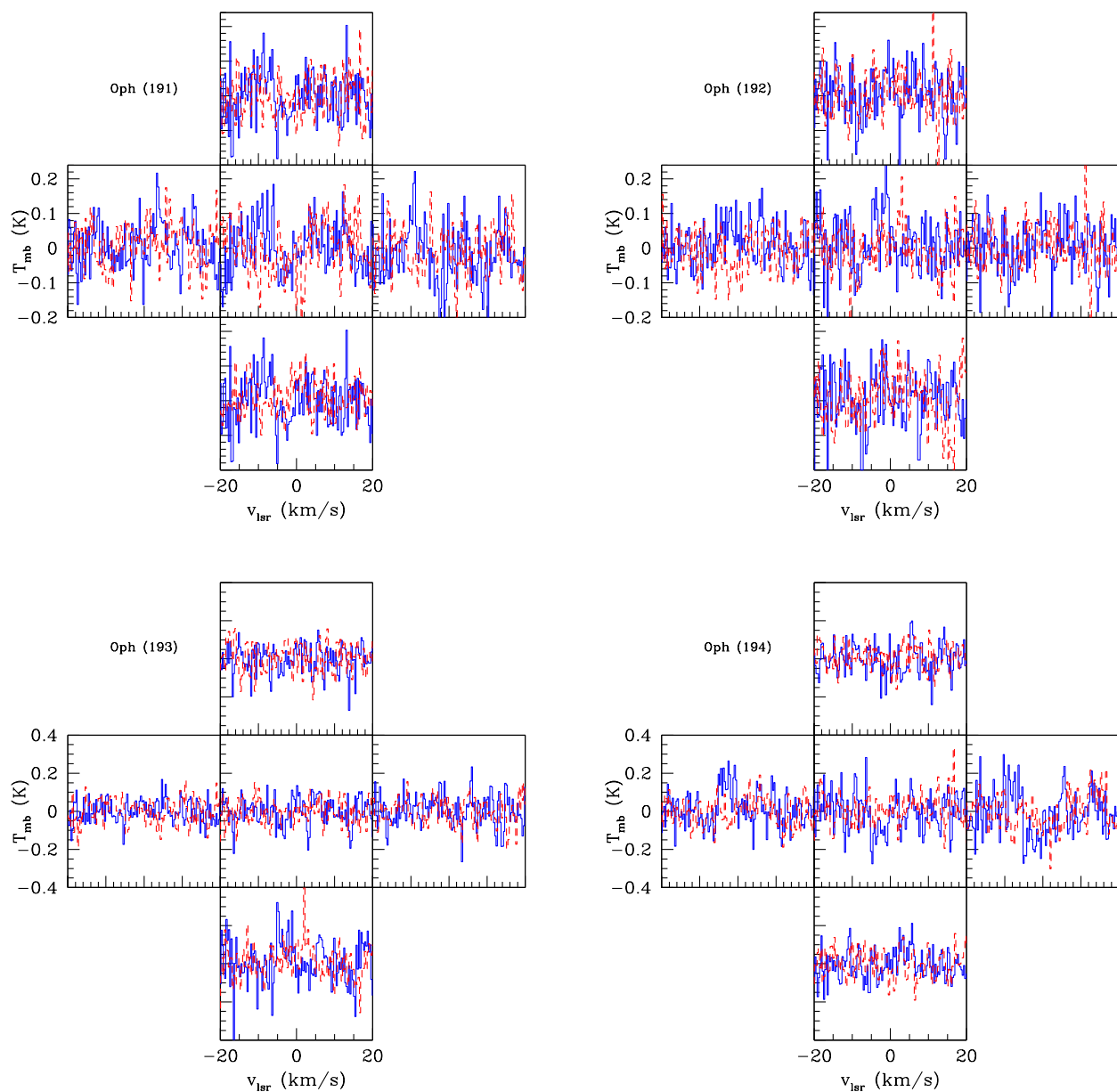


Fig. 8.— 5-point maps of ^{12}CO (solid line) and ^{13}CO (dashed line) 2 – 1 spectra toward the sources. The offset positions correspond to $30''$ shifts in RA and DEC from the protostar position. The source name is listed in the upper left of each 5-point map.

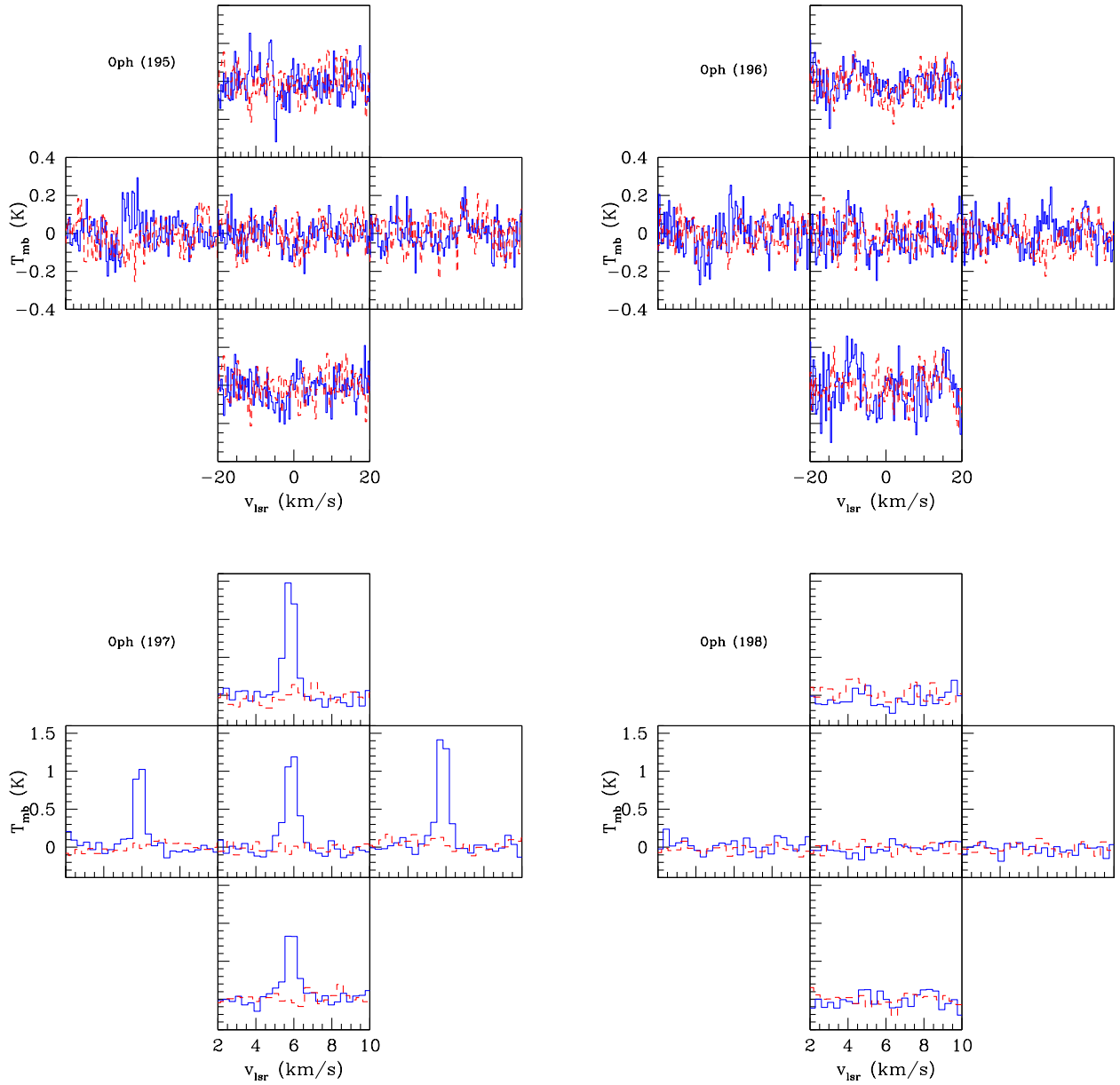


Fig. 9.— 5-point maps of ^{12}CO (solid line) and ^{13}CO (dashed line) 2 – 1 spectra toward the sources. The offset positions correspond to $30''$ shifts in RA and DEC from the protostar position. The source name is listed in the upper left of each 5-point map.

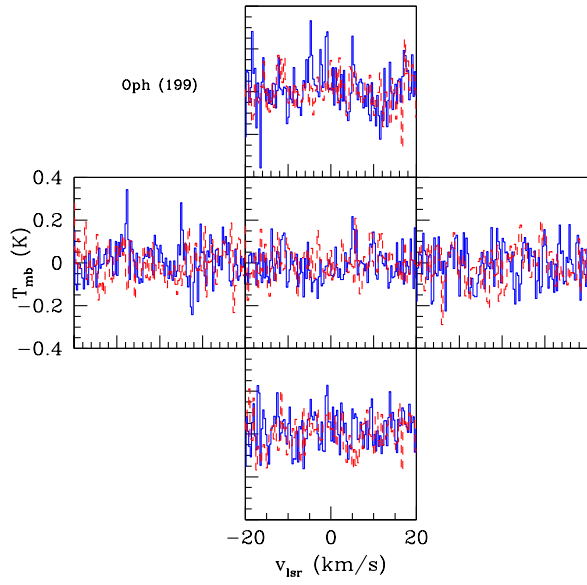


Fig. 10.— 5-point maps of ^{12}CO (solid line) and ^{13}CO (dashed line) 2 – 1 spectra toward the sources. The offset positions correspond to $30''$ shifts in RA and DEC from the protostar position. The source name is listed in the upper left of each 5-point map.

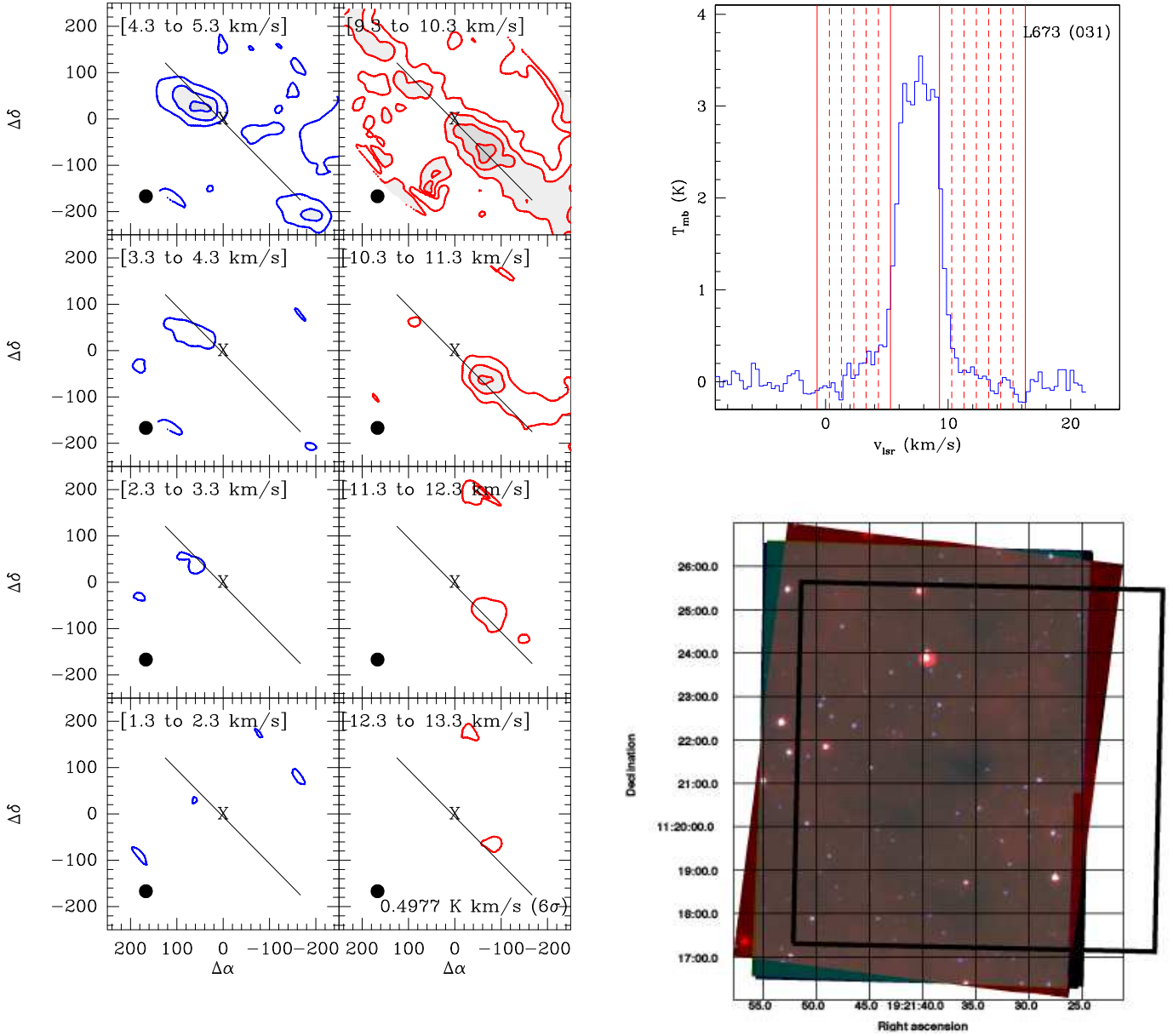


Fig. 11.— LEFT: Channel map of outflow emission from L673-7 (031). The left column shows emission from the blue wing while the right column shows emission from the red wing with velocity intervals listed at the top of each panel. Contours start at $3\sigma_I$. The direction of the outflow and position of the source are indicated. UPPER RIGHT: Velocity channels used to calculate outflow properties shown for the central spectrum. LOWER RIGHT: *Spitzer* 3 color image (4.5, 8.0, 24.0 μm) centered on L673-7. The solid box delineates the mapped region.

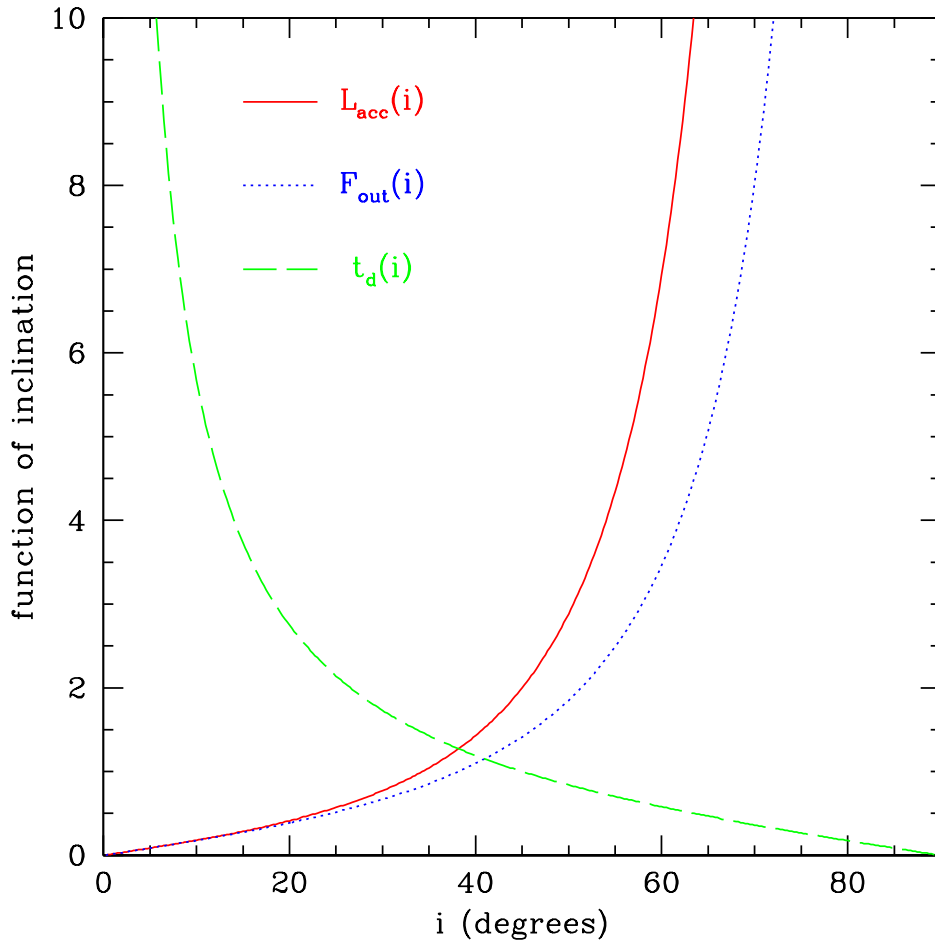


Fig. 12.— The dependence of inferred protostellar accretion luminosity L_{acc} , outflow force F_{out} , and the dynamical time t_d of the outflow with inclination of the outflow. Inclination is defined as the angle from the line-of-sight to the observer ($i = 0^\circ$ is an outflow aligned with the line-of-sight while $i = 90^\circ$ is perpendicular to the line-of-sight). The dynamical time of the outflow may change by a factor of 7.6 over a reasonable inclination range ($20 - 70^\circ$) while the outflow force and inferred protostellar accretion luminosity may change by factors 20.6 and 57.3 respectively over the same range.

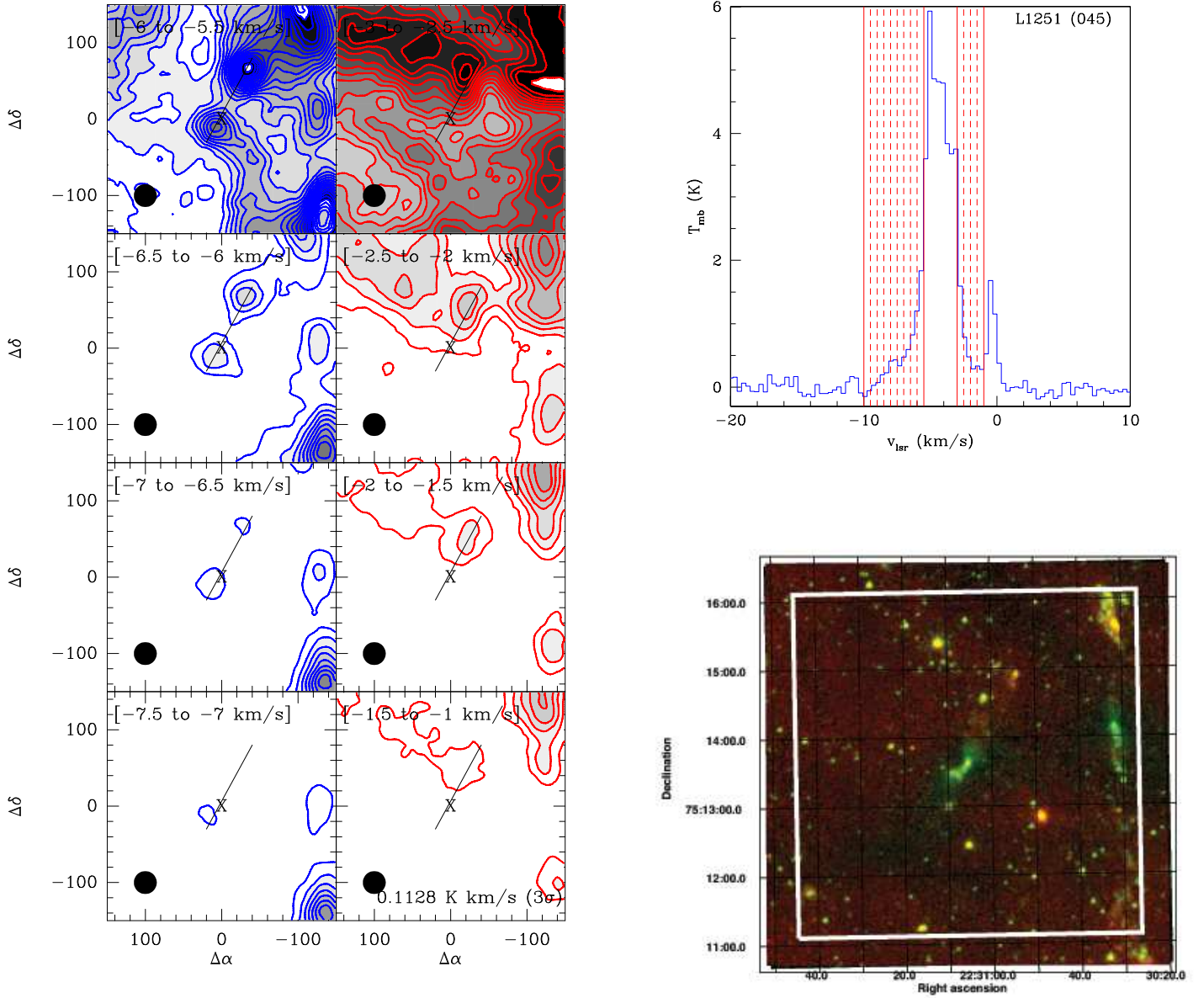


Fig. 13.— LEFT: Channel map of outflow emission from L1251-A. The left column shows emission from the blue wing while the right column shows emission from the red wing with velocity intervals listed at the top of each panel. Contours start at $3\sigma_I$. The direction of the outflow and position of the source are indicated. The strong outflow source L1251-A (044) is also seen along the eastern side of each panel. UPPER RIGHT: Velocity channels used to calculate outflow properties shown for the central spectrum. LOWER RIGHT: *Spitzer* 2 color image (4.6, 8.0 μm) centered on L1251A (045). The solid box delineates the mapped region. Shocked 4.6 μm emission (green) traces the directions of the outflow.

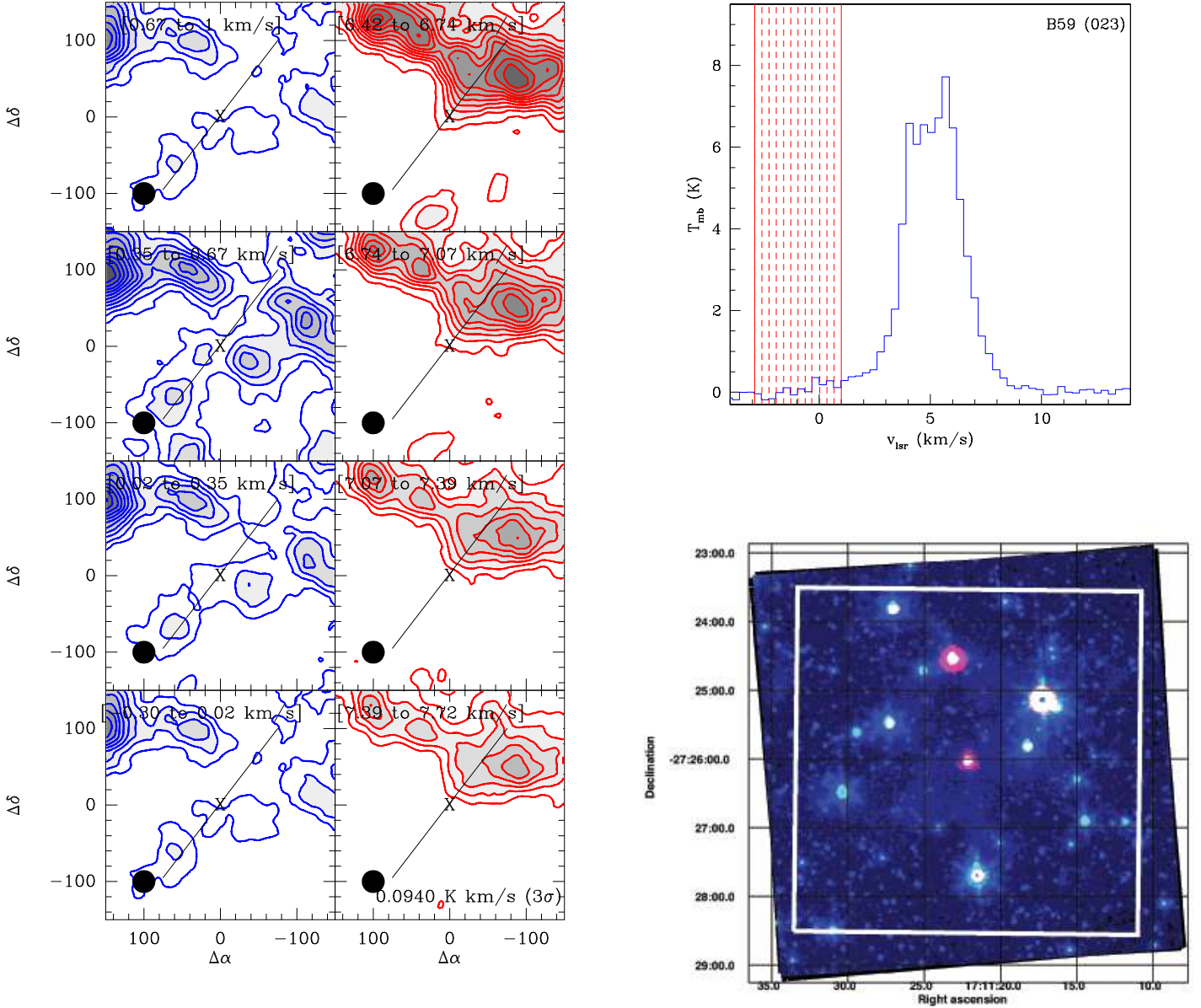


Fig. 14.— LEFT: Channel map of outflow emission from B59 (023). The left column shows emission from the blue wing with velocity intervals listed at the top of each panel. The right column shows emission from the red wing. Contours start at $3\sigma_I$. The strong outflow source IRAS17081-2721 is also seen along the northern side of each panel and may obscure the red lobe of the outflow. UPPER RIGHT: Velocity channels used to calculate outflow properties shown for the central spectrum. LOWER RIGHT: *Spitzer* 2 color image (4.6, 8.0 μm) centered on B59 (023). The solid box delineates the mapped region.

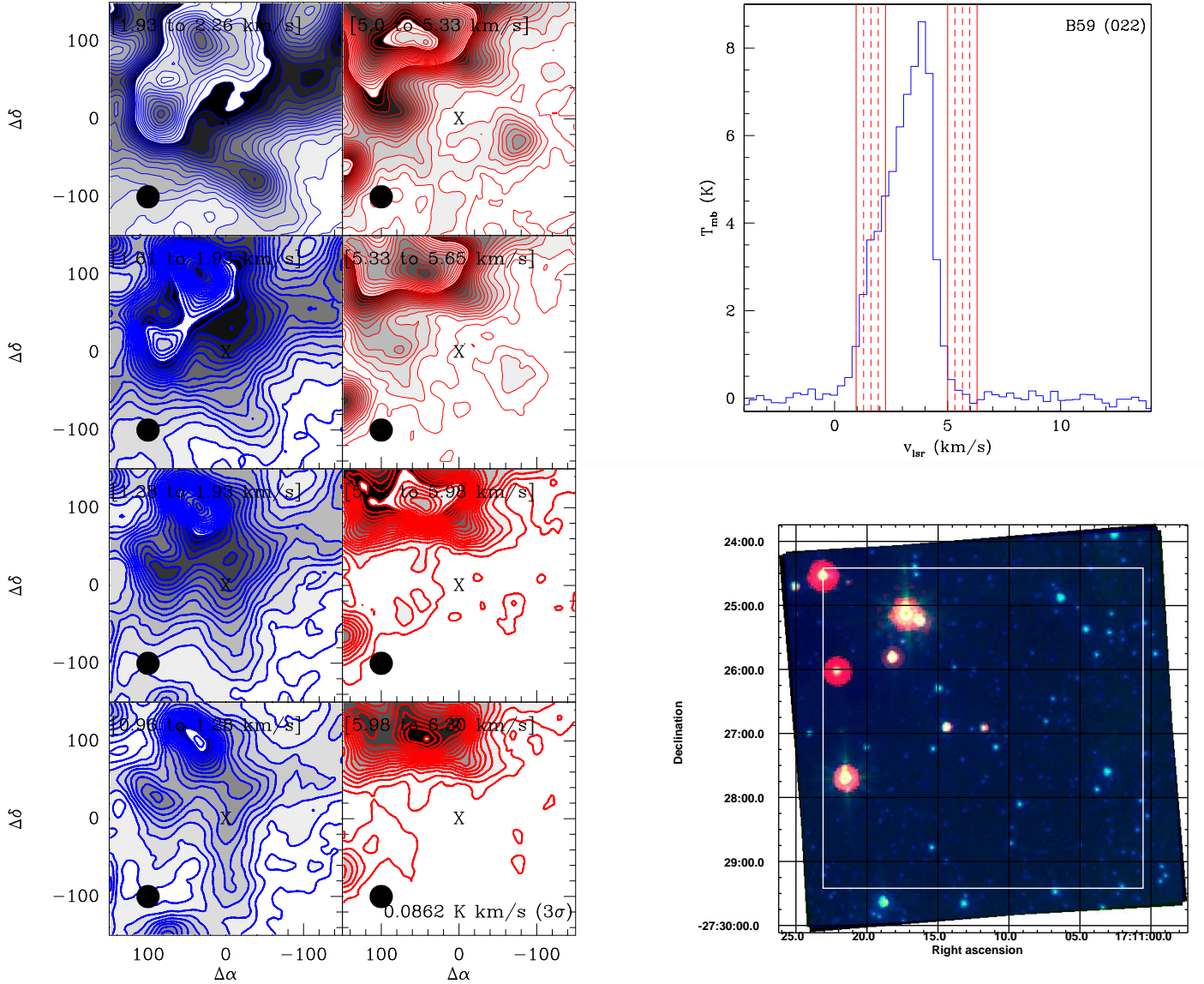


Fig. 15.— LEFT: Channel map of outflow emission from B59 (022). No outflow was detected around this source. The left column shows emission from the blue wing with velocity intervals listed at the top of each panel. The right column shows emission from the red wing. Contours start at $3\sigma_I$. The strong outflow source IRAS17081-2721 is also seen along the northern side of each panel. UPPER RIGHT: Velocity channels used to calculate outflow properties shown for the central spectrum. LOWER RIGHT: Three color (4.6, 8.0, 24.0 μm) *Spitzer* image centered on B59 (022). The solid box delineates the mapped region.

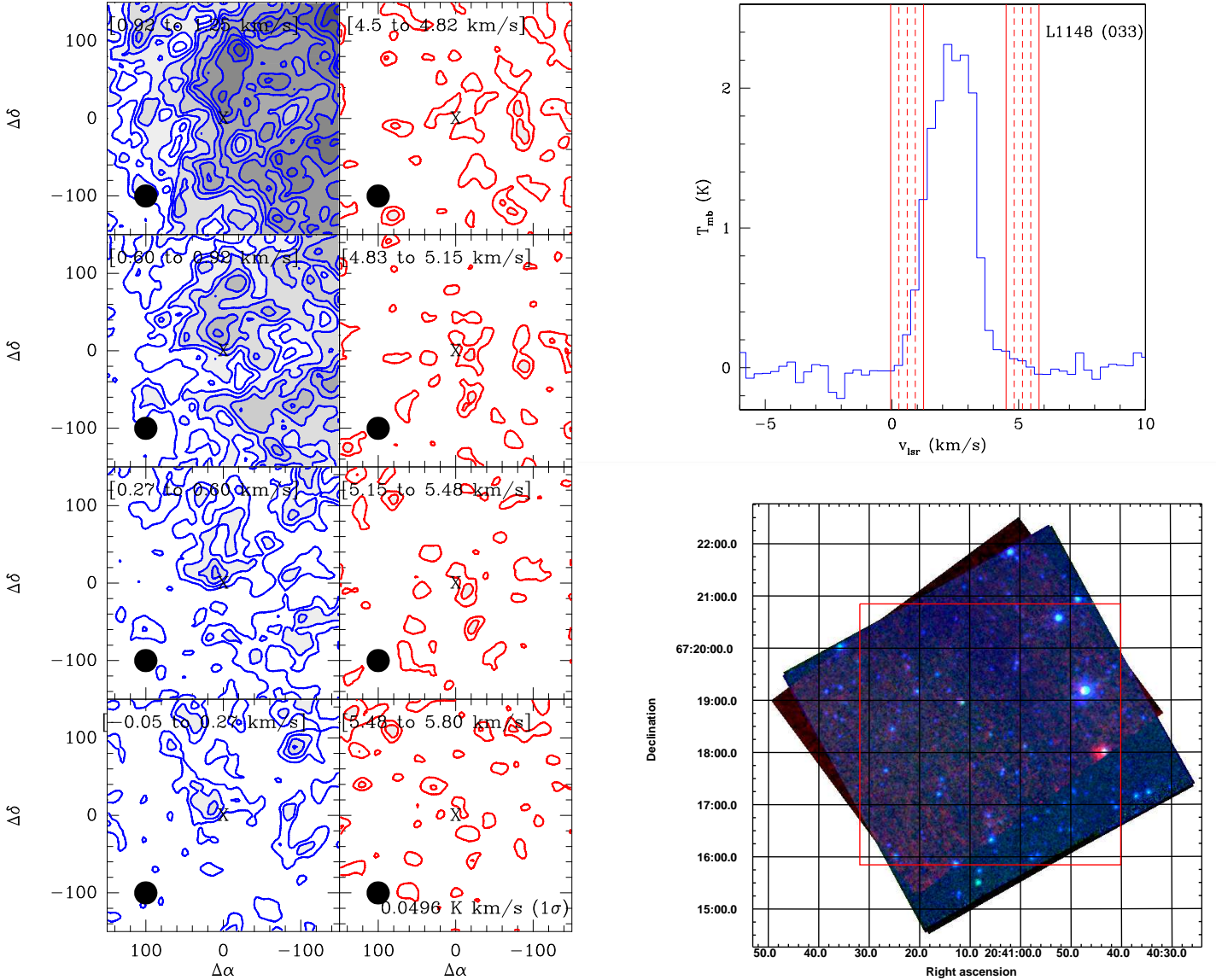


Fig. 16.— LEFT: Channel map of outflow emission from L1148 (033). No outflow was detected around this source. The left column shows emission from the blue wing with velocity intervals listed at the top of each panel. The right column shows emission from the red wing. Contours start at $3\sigma_I$. There is no distinctive outflow signature from the candidate protostar is seen. UPPER RIGHT: Velocity channels used to plot channel maps shown for the central spectrum. LOWER RIGHT: Three color (4.6, 8.0, 24.0 μm) *Spitzer* image centered on L1148 (033). The solid box delineates the mapped region.

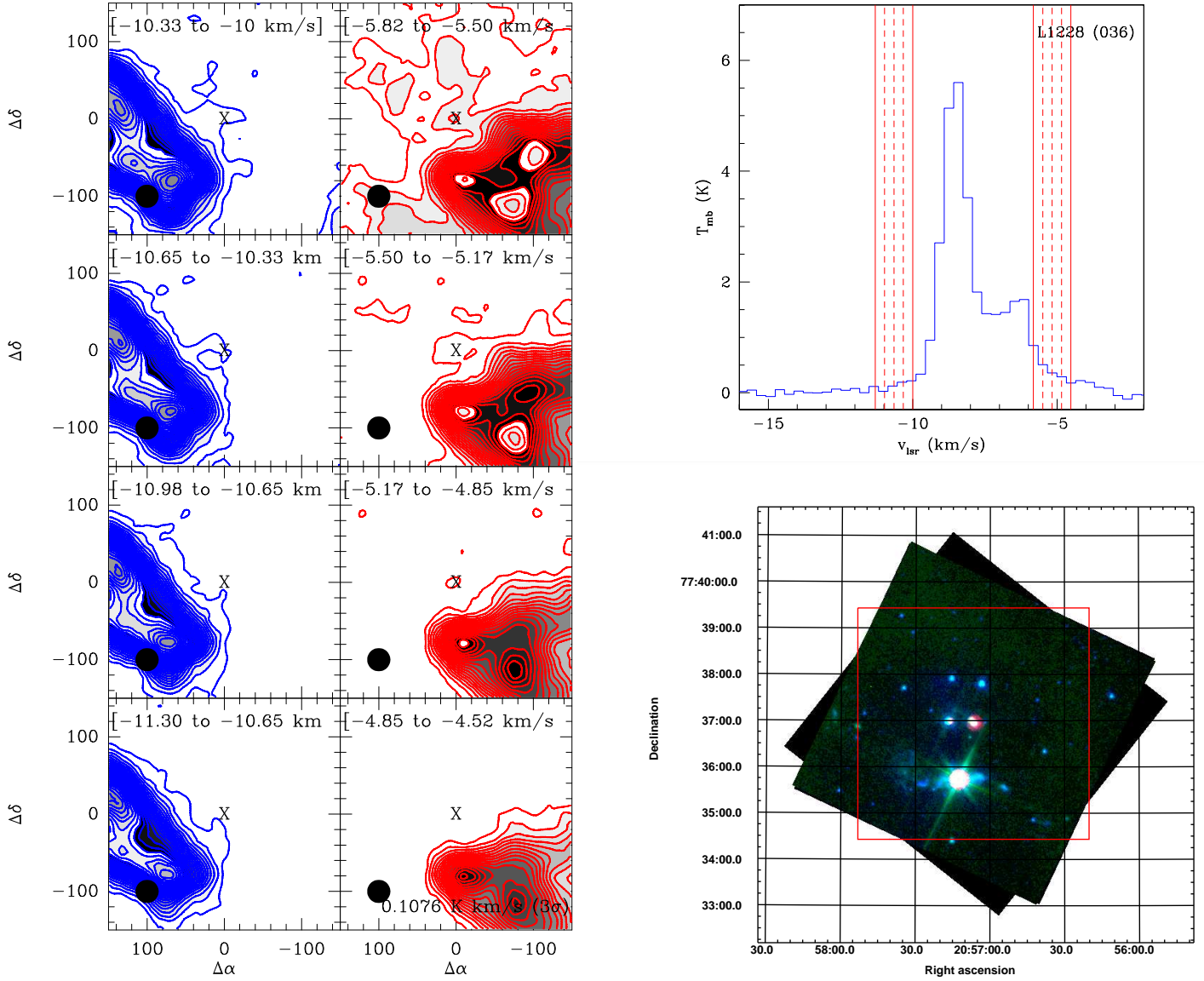


Fig. 17.— LEFT: Channel map of outflow emission from L1228 (036). No outflow was detected around this source. The left column shows emission from the blue wing with velocity intervals listed at the top of each panel. The right column shows emission from the red wing. Contours start at $3\sigma_I$. There is significant confusion in this region and no distinctive outflow signature from the candidate protostar is seen. UPPER RIGHT: Velocity channels used to plot channel maps shown for the central spectrum. LOWER RIGHT: Three color (4.6, 8.0, 24.0 μm) *Spitzer* image centered on L1228 (036). The solid box delineates the mapped region.

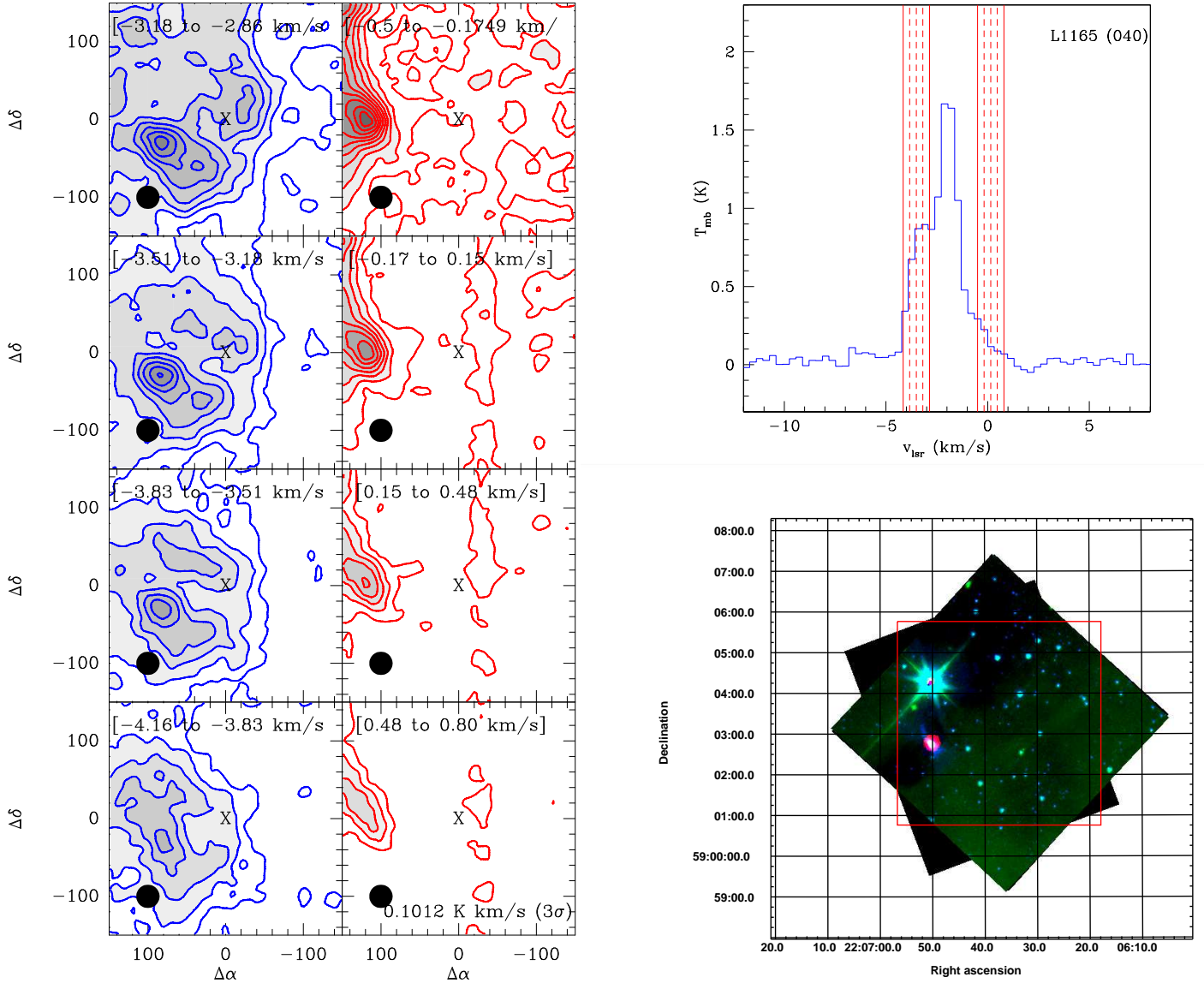


Fig. 18.— LEFT: Channel map of outflow emission from L1165 (040). No outflow was detected around this source. The left column shows emission from the blue wing with velocity intervals listed at the top of each panel. The right column shows emission from the red wing. Contours start at $3\sigma_I$. There is significant confusion in this region and no distinctive outflow signature from the candidate protostar is seen. UPPER RIGHT: Velocity channels used to plot channel maps shown for the central spectrum. LOWER RIGHT: Three color (4.6, 8.0, 24.0 μ m) *Spitzer* image centered on L1165 (040). The solid box delineates the mapped region.

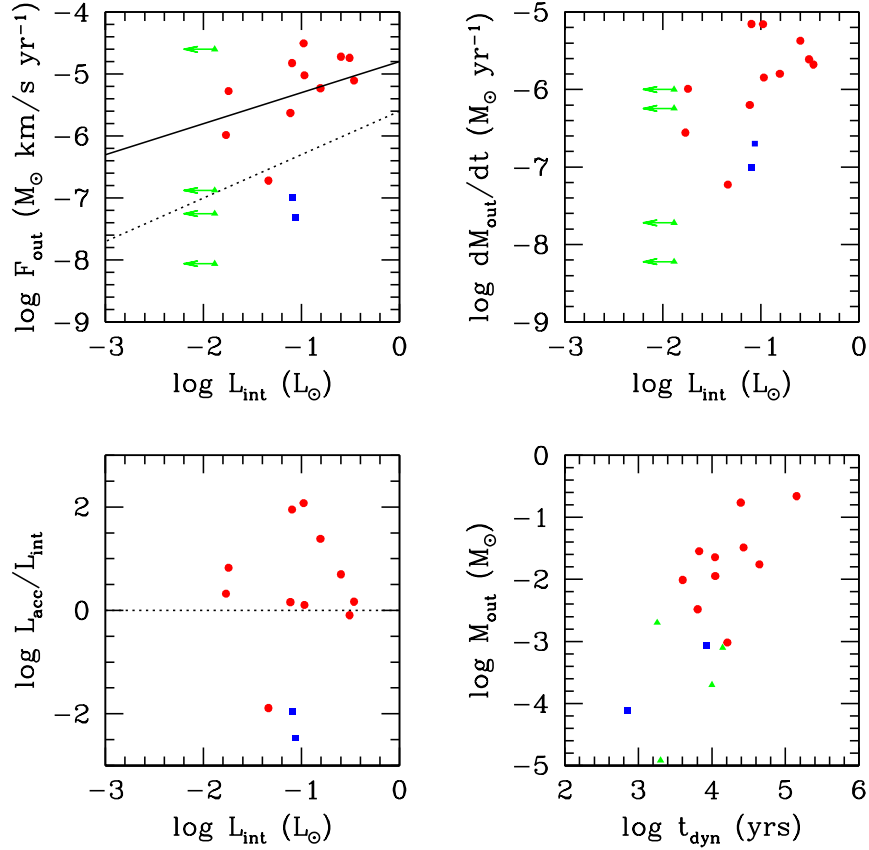


Fig. 19.— The outflow force vs. internal protostellar luminosity is shown in the upper left panel. Red circles denote single-dish detected outflow. Blue squares are detected with an interferometer only. Green triangles are first hydrostatic core candidates with upper limits on their internal luminosity. Data include the 3 outflows mapped in this survey plus data culled from the literature for all known VeLLO outflows and low-luminosity outflows in the Dunham et al. 2008 catalog (IRAM01491 André et al. 1999, MMS 126 Stanke et al. 2006, L1014 Shirley et al. 2007, L1448-IRS2E1 Chen et al. 2010, CB17 MMS Chen et al. 2012, Per 071 073 105 106 Curtis et al. 2010, L1251A-IRS3 Lee et al. 2010, L1148-IRS Kauffmann et al. 2011, Per-Bolo-58 Dunham et al. 2011, L1451-MM Pineda et al. 2011, LFAM 26 Nakamura et al. 2011). The solid line is the correlation for Class 0 sources in the Curtis et al. 2010 survey of Perseus while the dashed line is the correlation for Class I sources. The outflow mass rate is plotted versus internal luminosity in the upper right. The time average accretion luminosity (assuming $R = 3R_{\odot}$) vs. internal luminosity is plotted in the lower left. The dashed horizontal line denote where the ratio is equal to 1. The outflow mass is plotted vs. the dynamical timescale of the outflow in the lower right panel.

Table 1. Candidate Low-Luminosity Embedded Objects in the Cores^a

Source Number	Group ^b	Date Observed MJD-2450000	Spitzer Source Name ^c	c2d Core Region ^d	Dist. (pc)	RA (J2000)	Dec (J2000)	L_{IR}^e (L_{\odot})	D_{IRAS} (")	Nearest IRAS Source	HHT Obs. ^f
007	6	5170	J054443.94+090307.2	B35A	400 ± 40	05 44 43.94	+09 03 07.2	0.006	405.4	05417+0907	5-pt.
020	5	5242	J163705.11-353219.7	DC 3460+78	150 ± 20	16 37 05.11	-35 32 19.7	0.003	221.3	16335-3528	5-pt.
022	6	5242, 5592	J171111.83-272655.0	B59	125 ± 25	17 11 11.83	-27 26 55.0	0.024	125.9	17082-2724	OTF
023	3	5242, 5599	J171122.18-272602.0	B59	125 ± 25	17 11 22.18	-27 26 02.0	0.343	86.3	17081-2721	OTF
026	6	5171	J191744.28+191523.7	L723	200 ± 100	19 17 44.28	+19 15 23.7	0.048	225.4	19156+1906	5-pt.
027	1	5528	J192025.32+112217.4	L673	300 ± 100	19 20 25.32	+11 22 17.4	0.201	42.9	19180+1116	5-pt.
028	5	5529	J192025.92+112221.0	L673	300 ± 100	19 20 25.92	+11 22 21.0	0.168	52.5	19180+1116	5-pt.
030	3	5529	J192026.54+112025.4	L673	300 ± 100	19 20 26.54	+11 20 25.4	0.138	35.4	19180+1114	5-pt.
031	1	5171, 5172, 5179	J192134.82+112123.4	L673-7	300 ± 100	19 21 34.82	+11 21 23.4	0.017	427.6	19189+1109	OTF
032	3	5170	J204056.66+672304.9	L1148	325 ± 25	20 40 56.66	+67 23 04.9	0.081	222.3	20410+6710	5-pt.
033	6	5170, 5598	J204105.95+671820.9	L1148	325 ± 25	20 41 05.95	+67 18 20.9	0.003	250.9	20410+6710	OTF
034	6	5170	J204355.51+673850.3	L1155E	325 ± 25	20 43 55.51	+67 38 50.3	0.004	642.1	20423+6736	5-pt.
035	6	5170	J204427.17+673835.9	L1155E	325 ± 25	20 44 27.17	+67 38 35.9	0.004	768.6	20423+6736	5-pt.
036	6	5170, 5599	J205706.72+773656.2	L1228	200 ± 50	20 57 06.72	+77 36 56.2	0.199	72.7	20582+7724	OTF ^g
037	6	5170	J205707.85+773659.8	L1228	200 ± 50	20 57 07.85	+77 36 59.8	0.038	75.4	20582+7724	5-pt. ^g
039	6	5170	J220633.22+590232.6	L1165	300 ± 50	22 06 33.22	+59 02 32.6	0.030	135.6	22051+5848	5-pt. ₁
040	6	5529, 5592, 5598	J220637.27+590315.8	L1165	300 ± 50	22 06 37.27	+59 03 15.8	0.008	107.5	22051+5848	OTF
041	1	5170	J222807.42+690038.9	L1221	250 ± 50	22 28 07.42	+69 00 38.9	0.404	41.9	22266+6845	5-pt.
042	6	5170	J222933.39+751316.0	L1251	300 ± 50	22 29 33.39	+75 13 16.0	0.066	119.7	22290+7458	5-pt.
044	1	5171	J223031.94+751408.9	L1251	300 ± 50	22 30 31.94	+75 14 08.9	0.156	120.5	22290+7458	OTF
045	1	5171, 5184, 5599	J223105.59+751337.2	L1251	300 ± 50	22 31 05.59	+75 13 37.2	0.077	252.0	22290+7458	OTF
046	6	5171	J223514.06+751502.5	L1251	300 ± 50	22 35 14.06	+75 15 02.5	0.030	129.3	22343+7501	5-pt.
047	6	5171	J223731.13+751041.5	L1251	300 ± 50	22 37 31.13	+75 10 41.5	0.004	295.5	22376+7455	5-pt.
178	5	5592	J162135.57-224351.6	Ophiuchus	125 ± 25	16 21 35.57	-22 43 51.6	0.004	1467.3	16200-2251	5-pt.
179	5	5241	J162145.12-234231.7	Ophiuchus	125 ± 25	16 21 45.12	-23 42 31.7	0.033	246.9	16187-2339	5-pt.
181	3	5241	J162648.48-242838.6	Ophiuchus	125 ± 25	16 26 48.48	-24 28 38.6	0.103	366.6	16235-2416	5-pt.
183	3	5241	J162715.89-243843.1	Ophiuchus	125 ± 25	16 27 15.89	-24 38 43.1	0.440	163.5	16240-2430	5-pt.
186	5	5599	J162843.68-231918.1	Ophiuchus	125 ± 25	16 28 43.68	-23 19 18.1	0.000	516.2	16262-2317	5-pt.
187	5	5599	J163122.87-231655.2	Ophiuchus	125 ± 25	16 31 22.87	-23 16 55.2	0.003	1354.8	16275-2251	5-pt.
188	6	5241	J163131.25-242628.0	Ophiuchus	125 ± 25	16 31 31.25	-24 26 28.0	0.013	70.9	16285-2421	5-pt.
191	5	5241	J163502.45-235100.7	Ophiuchus	125 ± 25	16 35 02.45	-23 51 00.7	0.006	1074.3	16318-2402	5-pt.
192	5	5242	J164001.80-244429.0	Ophiuchus	125 ± 25	16 40 01.80	-24 44 29.0	0.004	447.9	16375-2439	5-pt.
193	5	5242	J164114.35-243758.1	Ophiuchus	125 ± 25	16 41 14.35	-24 37 58.1	0.007	539.7	16377-2426	5-pt.
194	5	5242	J164147.64-243030.2	Ophiuchus	125 ± 25	16 41 47.64	-24 30 30.2	0.005	591.5	16381-2419	5-pt.

Table 1—Continued

Source Number	Group ^b	Date Observed MJD-2450000	Spitzer Source Name ^c	c2d Core Region ^d	Dist. (pc)	RA (J2000)	Dec (J2000)	L_{IR}^e (L_{\odot})	D_{IRAS} (")	Nearest IRAS Source	HHT Obs. ^f
195	5	5255	J164206.74–233859.3	Ophiuchus	125 ± 25	16 42 06.74	–23 38 59.3	0.005	538.5	16384-2334	5-pt.
196	5	5255	J164301.87–245420.9	Ophiuchus	125 ± 25	16 43 01.87	–24 54 20.9	0.002	295.6	16403-2447	5-pt.
197	5	5255	J164305.88–242357.5	Ophiuchus	125 ± 25	16 43 05.88	–24 23 57.5	0.005	345.0	16396-2419	5-pt.
198	5	5242	J164433.26–233348.2	Ophiuchus	125 ± 25	16 44 33.26	–23 33 48.2	0.005	329.6	16411-2329	5-pt.
199	5	5242	J164512.50–233848.1	Ophiuchus	125 ± 25	16 45 12.50	–23 38 48.1	0.016	375.3	16420-2327	5-pt.

^aReproduced from Dunham et al. 2008.

^bGroup indicating likelihood of being an embedded protostar.

^cAll source names are preceded by the prefix “SSTc2d”.

^dName of the core region from Evans et al. (2007) in which this source is located.

^eIntegrated luminosity using all available detections between 1.25 (2MASS J-band) and 70 μm . Entries in italics denote that the calculation only extends to 24 μm due to no flux information available at 70 μm .

^fHHT Mapping mode. 5-pt. = 5 point map with 30'' spacing. OTF = On-the-fly map with 10'' row spacing.

Table 2. η_{pol} for Observing Shifts

MJD -2450000	V_{pol} LSB	H_{pol} LSB	V_{pol} USB	H_{pol} USB
5170	0.89	0.92	0.87	0.89
5172	0.97	0.94	0.94	0.90
5179	0.91	0.95	0.90	0.93
5184	0.88	0.92	0.87	0.89
5527	0.80	0.53	0.79	0.53
5242	0.99	...	0.94	...
5255	1.03	...	1.00	...
5592	0.67	0.76	0.65	0.76
5599	0.66	0.76	0.64	0.76

Table 3. Spectral properties for the center position of each source.

Source	$^{12}\text{CO } T_{pk}$ (K)	$^{12}\text{CO I}$ (K km/s)	$^{13}\text{CO } T_{pk}$	$^{13}\text{CO I}$ (K km/s)	$^{13}\text{CO}\Delta v$ (km/s)	Flags ^{a b}
B35A (007)	8.900 (0.034)	9.934 (0.047)	1.496 (0.041)	1.208 (0.072)	0.892 (0.004)	s
DC3460+78 (020)	2.717 (0.111)	9.934 (0.200)	... (0.090)	1.107 (0.166)	...	mc
B59 (022)	7.003 (0.089)	20.843 (0.160)	4.992 (0.072)	7.060 (0.119)	1.098 (0.012)	s bw
B59 (023)	6.551 (0.092)	10.439 (0.148)	4.986 (0.090)	9.811 (0.148)	1.549 (0.017)	s bw rw
L723 (026)	5.626 (0.096)	21.485 (0.197)	2.89 (0.097)	6.490 (0.179)	1.791 (0.052)	mc
L673 (027)	3.054 (0.050)	22.229 (0.127)	2.412 (0.038)	7.509 (0.066)	2.353 (0.018)	mc w?
L673 (028)	3.197 (0.046)	25.798 (0.128)	2.15 (0.048)	7.345 (0.093)	2.475 (0.027)	mc w?
L673 (030)	3.100 (0.073)	27.773 (0.186)	2.611 (0.060)	9.159 (0.116)	2.298 (0.031)	sa rw
L673-7 (031)	3.545 (0.073)	11.952 (0.150)	2.825 (0.059)	3.809 (0.103)	1.504 (0.038)	s bw rw
L1148 (032)	3.158 (0.040)	6.785 (0.072)	1.075 (0.042)	1.293 (0.065)	1.944 (0.015)	s
L1148 (033)	2.295 (0.050)	5.561 (0.086)	1.574 (0.039)	1.405 (0.060)	1.979 (0.022)	s
L1148 (034)	3.138 (0.038)	8.674 (0.069)	1.64 (0.045)	1.536 (0.070)	3.512 (0.024)	mc
L1148 (035)	3.826 (0.041)	9.599 (0.074)	1.357 (0.044)	1.619 (0.068)	3.215 (0.020)	mc
L1228 (036)	6.560 (0.056)	11.647 (0.111)	3.373 (0.040)	5.262 (0.066)	1.239 (0.084)	sa
L1228 (037)	6.894 (0.050)	12.018 (0.099)	3.546 (0.043)	5.543 (0.071)	1.199 (0.072)	sa
L1165 (039)	0.795 (0.076)	1.796 (0.156)	... (0.043)	... (0.242)	2.394 (0.127)	mc sa bw
L1165 (040)	1.667 (0.061)	5.290 (0.104)	0.7066 (0.038)	0.929 (0.063)	0.767 (0.035)	s
L1221 (041)	5.840 (0.045)	28.161 (0.123)	3.435 (0.056)	7.756 (0.113)	5.326 (0.033)	s
L1251 (042)	3.986 (0.072)	9.519 (0.116)	1.137 (0.049)	1.960 (0.099)	2.229 (0.022)	s bw rw
L1251 (044)	4.088 (0.048)	15.805 (0.102)	1.511 (0.050)	2.792 (0.082)	3.006 (0.021)	sa
L1251 (045)	5.220 (0.057)	16.160 (0.122)	1.603 (0.055)	2.992 (0.091)	2.612 (0.080)	mc
L1251 (046)	4.430 (0.061)	12.133 (0.120)	2.69 (0.056)	4.817 (0.092)	2.627 (0.005)	s
L1251 (047)	4.184 (0.051)	12.862 (0.101)	2.485 (0.046)	5.126 (0.076)	2.785 (0.014)	s
Oph (178)	0.161 (0.049)	0.392 (0.068)	... (0.077)	... (0.432)	...	mc
Oph (179)	15.910 (0.083)	35.408 (0.222)	12.42 (0.083)	13.553 (0.153)	0.973 (0.007)	mc
Oph (181)	16.610 (0.060)	59.199 (0.137)	12.51 (0.063)	23.853 (0.127)	1.816 (0.011)	s
Oph (183)	12.040 (0.086)	52.213 (0.196)	9.454 (0.059)	26.238 (0.109)	2.739 (0.010)	s
Oph (186)	7.149 (0.057)	16.297 (0.086)	0.268 (0.053)	0.701 (0.082)	1.685 (0.182)	s
Oph (187)	0.384 (0.055)	0.592 (0.083)	... (0.051)	... (0.287)
Oph (188)	0.505 (0.090)	1.086 (0.145)	... (0.075)	... (0.419)
Oph (191)	... (0.082)	... (0.536)	... (0.077)	... (0.432)
Oph (192)	... (0.083)	... (0.545)	... (0.076)	... (0.351)
Oph (193)	... (0.076)	... (0.498)	... (0.075)	... (0.417)
Oph (194)	... (0.102)	... (0.666)	... (0.104)	... (0.580)
Oph (195)	... (0.074)	... (0.484)	... (0.080)	... (0.444)
Oph (196)	... (0.099)	... (0.644)	... (0.082)	... (0.458)
Oph (197)	1.189 (0.081)	0.863 (0.131)	... (0.078)	... (0.438)	...	s
Oph (198)	... (0.082)	... (0.539)	... (0.095)	... (0.533)
Oph (199)	... (0.081)	... (0.531)	... (0.083)	... (0.463)

^aFlags indicating spectral features in ^{12}CO : rw and bw indicate evidence for red and blue wings, s is for single components, mc for multiple components, and sa for self absorbed peaks. See § 3.1.

^bEllipses indicate non-detections.

Table 4. Observed Outflow Properties

Quantity	Units	B59 (023)	L673-7 (031)	L1251-A (045)
M_{out}	$10^{-2} M_{\odot}$	2.279 ± 0.036	1.741 ± 0.022	3.265 ± 0.020
E_{out}	$10^{42} \text{ erg } \frac{1}{\cos^2 i}$	3.52 ± 0.37	0.99 ± 0.17	1.36 ± 0.13
P_{out}	$10^{32} \text{ g km s}^{-1} \frac{1}{\cos i}$	1.7372 ± 0.0016	$0.92491 \pm .00030$	1.266 ± 0.062
t_{dyn}	$10^4 \text{ yr } \frac{\cos i}{\sin i}$	1.10 ± 0.13	4.43 ± 0.23	2.69 ± 0.65
L_{out}	$10^{-3} L_{\odot} \frac{\sin i}{\cos^3 i}$	2.59 ± 0.14	0.182 ± 0.033	0.41 ± 0.11
F_{out}	$10^{-6} M_{\odot} \text{ km s}^{-1} \text{ yr}^{-1} \frac{\sin i}{\cos^2 i}$	7.86 ± 0.25	1.043 ± 0.054	2.35 ± 0.58
$\langle dM_{acc}/dt \rangle$	$10^{-7} M_{\odot} \text{ yr}^{-1} \frac{\sin i}{\cos^2 i}$	21.0 ± 2.5	2.78 ± 0.14	6.3 ± 1.5
M_{proto}	$10^{-2} M_{\odot} \frac{1}{\cos^2 i}$	2.32 ± 0.39	1.233 ± 0.090	1.69 ± 0.58
L_{acc}	$L_{\odot} \frac{\sin i}{\cos^3 i}$	0.51 ± 0.10	0.0357 ± 0.0032	0.111 ± 0.047